JOURNAL OF GEOPHYSICAL RESEARCH, VOL. ???, XXXX, DOI:10.1029/,

The effect of ring current electron scattering rates on magnetosphere-ionosphere coupling

N. J. Perlongo,[1] A. J. Ridley,[1] M .W. Liemohn,[1] R. M. Katus[2]

Corresponding author: Department of Climate and Space Sciences and Engineering, University of Michigan, Ann Arbor, Michigan, USA. (nperlong@umich.edu)

[1]Department of Climate and Space Sciences and Engineering, University of Michigan, Ann Arbor, Michigan, USA.

[2]Department of Mathematics, Eastern Michigan University, Ypsilanti, Michigan, USA.

Abstract.

This simulation study investigated the electrodynamic impact of varying descriptions of the diffuse aurora on the magnetosphere-ionosphere (M-I) system. Pitch angle diffusion caused by waves in the inner magnetosphere is the primary source term for the diffuse aurora, especially during storm time. The magnetic local time (MLT) and storm dependent electrodynamic impacts of the diffuse aurora were analyzed using a comparison between a new self-consistent version of the Hot Electron Ion Drift Integrator (HEIDI) with varying electron scattering rates and real geomagnetic storm events. The results were compared with Dst and hemispheric power indices, as well as auroral electron flux and cross-track plasma velocity observations. It was found that changing the maximum lifetime of electrons in the ring current by 2-6 hours can alter electric fields in the nightside ionosphere by up to 26%. The lifetime also strongly influenced the location of the aurora, but the model generally produced aurora equatorward of observations.

1. Introduction

The ring current carries the majority of the energy density and plasma pressure in the magnetosphere, making it an extremely important plasma population in the magnetosphere-ionosphere (M-I) system. An accurate description of the ring current is therefore essential for geophysics systems research as well as space weather applications [*Daglis et al.*, 2009]. The majority of the energy content in the ring current is carried by protons due to their long lifetimes. The timescale for protons can be measured in days, where electrons may last only minutes or hours depending on L-shell and energy [*Chen et al.*, 2015]. Despite this, the storm time electron ring current has been found to constitute up to 25% of the ring current energy density [*Frank*, 1967; *Liu et al.*, 2005; *Jordanova and Miyoshi*, 2005].

Some electrons are predominately lost to the upper atmosphere via pitch angle scattering, primarily due to waves in the inner magnetosphere [e.g *Shprits et al.*, 2008a, b; *Thorne et al.*, 2010]. The types of waves responsible for such scattering have been found to be dependent on location. Electron cyclotron harmonic waves are dominant beyond 8 R_E [*Ni et al.*, 2012], while whistler chorus waves on the nightside are the primary cause of diffuse auroral electron precipitation closer to the Earth [*Thorne et al.*, 2010; *Ni et al.*, 2011a, b]. Plasmaspheric hiss also contributes to loss [*Lyons et al.*, 1972; *Albert*, 1994]. Interaction with these waves cause the velocity of the electron parallel to the magnetic field to increase such that its mirror point reaches a low enough altitude where it can collide with the upper atmosphere before bouncing back to the magnetosphere [*Kennel*, 1969;

Lyons et al., 1972]. The pitch-angle distributions resulting in precipitation are known as loss cone distributions.

The inclusion of these wave-particle interactions in ring current models is difficult since measurements of wave distributions, amplitudes, and frequencies are typically not available in tandem with plasma density observations [*Chen et al.*, 2015]. Consequently, a number of empirical models have been developed to approximate the pitch angle scattering rates. The first of these assumed strong scattering in all regions [*Schulz*, 1974]. Strong scattering is defined as when the pitch angle diffusion coefficient is much greater than $\alpha_c^2\Omega$, where α_c is the particle's pitch angle and Ω is its bounce frequency [*Kennel*, 1969]. The mean lifetime of a particle then approaches a minimum value, τ, which is dependent on the pitch angle, but not the diffusion coefficient [*Schulz*, 1974].

More recent plasma sheet particle and wave observations have shown that pitch angle diffusion is not strong everywhere [*Schumaker et al.*, 1989; *Gough et al.*, 1979; *Belmont et al.*, 1983; *Roeder and Koons*, 1989; *Meredith et al.*, 1999, 2000]. Simulations with only strong pitch angle diffusion have also demonstrated too high of a scattering rate in this limit [*Chen and Schulz*, 2001; *Chen et al.*, 2005, 2015]. In light of this, models were developed where the pitch angle diffusion transitions from strong to weak closer to the Earth [*Chen and Schulz*, 2001; *Chen et al.*, 2005], but without dependence on geomagnetic activity. Chorus wave scattering electron lifetimes were then parametrized on the dayside and nightside which varied by energy, geocentric distance, as well as the Kp index [*Gu et al.*, 2012; *Orlova and Shprits*, 2014]. Plasmaspheric hiss electron losses were similarly parametrized by *Orlova and Shprits* [2014] and *Orlova et al.* [2016].

The diffuse aurora resulting from ring current electron loss produces conductivity enhancements in the ionosphere - a key component for M-I electrodynamics. Since the divergence of total current in the M-I system must be zero, intensification's of the ring current driven field-aligned currents (FACs) in to and out of the ionosphere [*Wolf et al.*, 1982]. Hall and Pedersen conductivities regulate the potential pattern in the ionosphere, which then map back along field lines to the magnetosphere [*Nopper and Carovillano*, 1978], driving electric fields and establishing a feedback loop [*Vasyliunas*, 1970]. The resultant magnetospheric convection electric field drives particle transport in the ring current and the process repeats itself [*Ebihara et al.*, 2004; *Liemohn et al.*, 2005]. Often during geomagnetic storms, the FAC system cannot intensify quickly enough to regulate the increase in ring current plasma pressure, resulting in ionospheric electric fields equator-ward of the auroral oval known as penetration electric fields (PEFs) [e.g. *Burke*, 2007]. Reviews of the known relationships between PEF and the M-I system are given in *Huang et al.* [2007] and *Wolf et al.* [2007].

Plasma injection to the ring current from ionospheric outflow has also been shown to influence electrodynamics in the M-I system [*Winglee et al.*, 2002; *Yu and Ridley*, 2013; *Ilie et al.*, 2015; *Welling et al.*, 2015a]. Simulation studies have revealed that heavy ion outflow can create stronger azimuthal pressure gradients in the ring current, leading to FAC intensification that further enhances the electric fields and subsequent outflow [*Kronberg et al.*, 2014; *Welling et al.*, 2015b]. Completely describing these processes would require a global ionosphere/thermosphere model that is fully (two-way) coupled to a kinetic inner magnetosphere model. For the magnetosphere, this coupling would also mean a more accurate calculation of the electric field, since ionosphere/thermosphere chemistry and transport can greatly affect conductances [*Deng et al.*, 1991; *Peymirat*, 2002; *Garner et al.*, 2007]. For the ionosphere, the coupling would improve the description of the aurora and electric fields driven by the inner magnetosphere, leading to a more accurate model of ionosphere/thermosphere morphology. While this study ignores these effects, they should be included in future model developments.

Encompassing all of the M-I electrodynamic feedback physics in a self-consistent manner has been a longstanding challenge in the ring current modeling community. For many years, models used plasma sheet convective electric fields driven by analytical models such as Volland-Stern [*Volland*, 1973; *Stern*, 1975], or empirically derived potentials from, for example, the Weimer models [*Weimer*, 1996, 2001, 2005], resulting in many studies about the storm-time inner magnetospheric plasma [e.g. *Fok and Moore*, 1997; *Liemohn et al.*, 2001a; *Kozyra et al.*, 2002; *Jordanova*, 2003; *Chen et al.*, 2003]. The need for a self-consistent electric field was then addressed by including some description of the ionospheric conductance [*Wolf et al.*, 1982; *Toffoletto et al.*, 2003; *Fok et al.*, 2001; *Ridley and Liemohn*, 2002]. Since depressions in the Earth's magnetic field from ring current intensification's influence the gradient curvature drift of ring current particles [*Ebihara and Ejiri*, 2000], many models now have a self-consistent description of the magnetic field as well [*Lemon et al.*, 2004; *Zaharia et al.*, 2006; *Ilie et al.*, 2012; *Fok et al.*, 2014; *Jordanova et al.*, 2014].

Models are now being updated to self-consistently calculate the convection electric field while incorporating realistic ionospheric electrodynamics based on particle precipitation from the ring current. The Comprehensive Inner Magnetosphere-Ionosphere model (CIMI) [*Fok et al.*, 2014] was recently developed by integrating the Comprehensive Ring Current

Model (CRCM) [*Fok et al.*, 2001] and the Radiation Belt Electron (RBE) model [*Fok et al.*, 2011]. *Fok et al.* [2014] used CIMI to investigate the ionosphere's influence on particle pitch angle diffusion into the loss cone finding an especially large impact on MeV electron fluxes. *Chen et al.* [2015] compared electron scattering descriptions at geosynchronous orbit using a similar configuration of the self-consistent aurora. This study expanded on the model from *Ridley and Liemohn* [2002] by using the diffuse aurora produced by electron scattering as the primary source for conductance instead of a relationship with the FAC's.

Yu et al. [2016] compared a diffusion coefficient method [*Jordanova et al.*, 2008] to the electron lifetime loss method described here. They developed the Ring current-Atmosphere interaction Model with Self-Consistent Magnetic field (RAM-SCB) [*Jordanova and Miyoshi*, 2005; *Zaharia et al.*, 2010] to include both loss methods and investigated their effect on electron dynamics and M-I coupling. For a particular storm, they found that the diffusion coefficient method better agreed with observed precipitation fluxes.

In this study, the magnetic local time (MLT) and storm dependent electrodynamic impacts of the diffuse aurora were investigated using a comparison between the Hot Electron Ion Drift Integrator (HEIDI) model [*Liemohn et al.*, 2001b, 2005, 2006] with varying electron lifetimes and auroral observations. While previous studies have focused on the magnetospheric repercussions of the improved M-I electrodynamics, the emphasis here is on the ionospheric electric fields and aurora for the electron lifetime loss method only. These modeling efforts are a first step towards coupling with a global ionosphere-thermosphere model.

2. Model Description

A schematic of the model configuration is shown in Figure 1. The magnetosphere-ionosphere-thermosphere system is described by a number of models working together in an ad-hoc framework. First, ion and electron distributions in the inner magnetosphere are solved for using HEIDI. This is a kinetic ring current model that solves the time-dependent, gyration, bounce averaged kinetic equation for H^+, O^+, He^+, and e^- plasma species, though He^+ was not used for this study. The energy range of the species varies from a few eV to hundreds of keV. The model includes convective and magnetic gradient-curvature drift, losses due to Coulomb collisions, charge exchange, and atmospheric loss [*Liemohn et al.*, 2010]. HEIDI now includes a self-consistent auroral model by using the Ridley Ionosphere Model (RIM) [*Ridley and Liemohn*, 2002; *Ridley et al.*, 2004] with input from the field aligned currents and aurora from the ring current. The outer boundary of HEIDI is located at geosynchronous orbit where input is given by observed particle fluxes by the multiple-particle analyzer (MPA) [*McComas et al.*, 1993] and Synchronous Orbiting Particle Analyzer (SOPA) [*Belian et al.*, 1992] instruments from Los Alamos National Laboratory (LANL). The composition of the particles was derived using the empirical Young relationships provided by *Young et al.* [1982]. This version of HEIDI uses a static dipole magnetic field.

The electrons scattered in to the loss cone by HEIDI were used to calculate ionospheric conductances using the formulation by *Robinson et al.* [1987]:

$$\Sigma_P = \frac{40\overline{E}}{16+\overline{E}^2}\phi_E^{1/2} \qquad\qquad \frac{\Sigma_H}{\Sigma_P} = 0.45(\overline{E})^{0.85} \tag{1}$$

where Σ_H and Σ_P are the Hall and Pedersen conductances, $\overline{E}$ is the average energy in keV and ϕ_E is the energy flux in ergs cm^{-2} s^{-1}. *Kaeppler et al.* [2015] recently used incoherent scatter radar observations to verify the Robinson et al. formulas, finding good agreement with Pedersen conductance. They also updated the relation to be even more accurate for hall conductances, which could be used in future studies.

Since the outer boundary of HEIDI is at geosynchronous orbit, the self-consistent coupling could only occur below the footprint of the magnetic field lines there, at 67° magnetic latitude. Empirical models were used poleward of this boundary to complete the coupling. Driven by the SuperMAG Auroral Electrojet index [*Newell and Gjerloev*, 2011], the Ovation SME [*Mitchell et al.*, 2013] gave a smooth and relatively accurate description of the aurora. The Weimer electric potential model [*Weimer*, 2005] was also used to specify the electric potential above the 67° boundary and was driven by the upstream solar wind conditions observed from the ACE spacecraft [*McComas et al.*, 1998; *Smith et al.*, 1998].

The inclusion of these empirical models created sharp boundaries between self-consistently calculated values and the empirical models. As such, a smoothing was applied so that erroneous electric field intensification's did not arise along this boundary. Furthermore, the magnetospheric origin of the aurora often resides tailward of geosynchronous orbit. The Ovation model was solely used during these times for a more realistic auroral specification in the ionosphere. As the hemispheric power originating from the ring current increased, the contribution of the Ovation aurora was decreased linearly until only the self-consistent version remained. The self-consistent contribution began when the hemispheric power reached 10 GW and the Ovation contribution decreased to 0 GW when the total hemispheric power reached 40 GW.

In addition to the Hall and Pedersen conductances, the region 2 FACs were passed to RIM to solve for the electric potentials below 67°. The FACs are calculated numerically from local pressures in HEIDI [*Liemohn et al.*, 2001b].

Given the FAC, ($J_{\|}$), the height-integrated Hall and Pedersen conductivity tensor $\overline{\Sigma}$ and the magnetic dip angle I, the electric potential, ϕ, may be found by solving

$$\bigtriangledown \cdot (-\overline{\Sigma} \bigtriangledown \phi) = J_{\|} \sin I. \quad (2)$$

This equation implies that when FACs flow into regions of lower conductivity, the electric field must increase to ensure current continuity. The electric potentials are then passed back to HEIDI to drive the convective electric field in the ring current. This completes the self-consistent electric field model in HEIDI. The plasma populations of the HEIDI simulations are initialized by those of a previous simulation under nominal solar wind and magnetosphere conditions. All of the simulations were run for a period of at least 24 hours before storm onset to remove erroneous contributions from this initial condition.

A limitation of the model arises by not including proton precipitation in the conductance calculations. The conductance produced by their precipitation in the sub-auroral region has been found to be on the order of several mhos [*Galand and Richmond*, 2001; *Zou et al.*, 2014]. Conductance resulting from precipitating hot ions has also been shown to distort the potential pattern [*Khazanov et al.*, 2003]. Our model may therefore be underestimating the conductance in this region, potentially leading to a stronger electric field mapping back to the magnetosphere. Furthermore, the model does not include contributions from discrete auroral arcs or direct injections from the magnetosphere such as in the cusp region. While the majority of the conductance still comes from the diffuse electron aurora, these types of precipitation should be included in the future for a more accurate description.

The model presented here is currently one-way coupled with the global ionosphere thermosphere model (GITM) [*Ridley et al.*, 2006], which can be used to integrate the thermosphere in to the system. In the future, the self-consistent aurora from this version of HEIDI will be imported to the other version with a self-consistent magnetic field [*Ilie et al.*, 2012] coupled with the Space Weather Modeling Framework (SWMF) [*Tóth et al.*, 2005, 2012].

3. Methodology

HEIDI was run for 4 different storms, each with 4 scattering rate descriptions, for a total of 16 simulations. The basis of the loss model used originates directly from the work of *Chen and Schulz* [2001]; *Chen et al.* [2005] and *Schulz* [1974]. The model is such that the loss rate, $\overline{\lambda}(\varphi)$, transitions from strong to weak pitch-angle diffusion by

$$\overline{\lambda}(\varphi, R, E) = \frac{\lambda(\varphi, R, E)}{1 + \lambda(\varphi, R, E)\tau}, \quad (3)$$

where τ is the lifetime against strong diffusion, φ is the MLT, and λ is the scattering rate as a function of MLT (φ), energy (E), and geocentric distance (R) [*Chen et al.*, 2005]. Note that this relationship does not include a dependence on magnetic activity, which can change the location of the plasmapause [*Moldwin et al.*, 2002; *Katus et al.*, 2015] and scattering from enhanced wave amplitudes [*Meredith et al.*, 2004; *Miyoshi et al.*, 2006].

As *Chen et al.* [2005] demonstrated, the resulting lifetimes increase as particles move towards the Earth. This contrasts that of strong diffusion, where the lifetimes become increasingly short at low L-shells. In fact, the lifetimes increase so much in the weak diffusion limit that the loss is too little when compared with observations at geosynchronous orbit [*Chen et al.*, 2015]. To remedy this, an upper limit, τ_{max} was introduced to the scattering rates. For this study, τ_{max} was set to 8 hours, 4 hours, and 2 hours. Additionally, an energy dependent functional form was used where the lifetime in hours was given by,

$$\tau_{max} = 10(E)^{-0.5}, \tag{4}$$

where E is the particle energy in KeV. This formula was derived by comparing HEIDI electron fluxes at geosynchronous orbit to observations for different τ_{max} values. While the other τ_{max} values were arbitrarily chosen, the purpose of this was to demonstrate the importance of the electron scattering rate description on the ability of the model to reproduce auroral observations.

A test simulation with strong scattering everywhere was also done for each storm. In this case, the electrons were lost so quickly and close to the outer boundary that they did not have the chance to gain energy adiabatically by moving towards the Earth into a region of higher magnetic field strength. The result of this was an extremely low energy flux throughout the domain. These simulations resulted in the model defaulting to empirical results, so they are not shown in this paper.

To get a better understanding of the influence of the scattering rates, the model was run for 4 different storms. The storms were chosen to vary in strength and type, all while ensuring data availability. These include two co-rotating interaction regions (CIR) storms and two coronal mass ejection (CME) events. The storms were identified using the extensive list compiled by *Zhang et al.* [2007] of all the storms during solar cycle 23 in which the Dst dropped below -100 nT. A synopsis of the storms is given in Table 1. One weaker and one stronger storm was chosen for each type. The season was kept constant, as well as the UT of the main phase between storms of similar strength.

4. Results

4.1. Dst

The strength of the ring current is often measured using the disturbance storm time (Dst) index, which is calculated from the reduction of Earth's magnetic field observed at low-latitude magnetometers [*Sugiura et al.*, 1991]. In this study, the results are compared to the Dst^* index from both the Kyoto World Data Center and the United States Geological Survey (USGS) [*Love and Gannon*, 2009; *Gannon and Love*, 2011]. The Dst^* index more accurately describes the storm time ring current by removing from the Dst index the contributions from the magnetopause current, induced currents in the conducting Earth, and the quiet time ring current [*Ebihara and Ejiri*, 1998; *Kozyra et al.*, 1998; *Liemohn et al.*, 2001a; *Katus et al.*, 2015]. The model calculates Dst^* using the Dessler-Parker-Sckopke relationship [*Dessler and Parker*, 1959; *Sckopke*, 1966] given by

$$Dst^* = -3.98 \times 10^{-30} E_{RC} \tag{5}$$

where E_{RC} is the total modeled ring current energy in KeV and Dst^* is in nT.

A comparison of the Dst^* for all of the simulations is shown in Figure 2. The dashed black and purple lines represent the observed values. The dark grey line, with the strongest Dst^*_{min}, is an additional run performed using the empirically driven model with the Volland-Stern (V-S) electric field [*Volland*, 1973; *Stern*, 1975]. The remaining colored lines correspond to the results of simulations using different electron loss rate descriptions.

The self-consistent version of HEIDI produced a smaller Dst^* drop with little variation of the results between simulations using different τ_{max} values. This was to be expected, as electrons generally constitute a small percentage of the ring current energy density [*Frank*, 1967; *Liu et al.*, 2005; *Jordanova and Miyoshi*, 2005]. There is no difference between these runs before the storms, since the aurora during this time was derived from the same empirical model. Storm B was the only storm with a notable difference in the Dst^*. Here the Dst^*_{min} was -94 nT for a τ_{max} of 2 hours, -83 nT for the energy dependent τ_{max}, -74 nT for a τ_{max} of 8 hours, and -72 for a τ_{max} of 4 hours. While the Dst^* was underestimated by an average of about 20 nT during the main phase of the storm, the magnitude was captured better throughout the main phase of storms A and B. However, the simulations of storms C and D missed the minimum by over 40 nT. In storms B and D, the self-consistent runs were more accurate in the timing of the minimum peak in Dst^*, but then recovered at a slower rate than the observations. While more storms would need to be run to determine if the model updates improve the Dst^* results, these simulations demonstrate that this model version performs reasonably well at capturing Dst^* compared to the model driven by V-S.

4.2. Auroral Location and Strength

The location and strength of the simulated aurora was compared to Global Ultraviolet Imager (GUVI) data from the Thermosphere, Ionosphere, Mesosphere Energetics and Dynamics (TIMED) satellite [*Paxton et al.*, 1999, 2004; *Christensen*, 2003]. From a circular orbit of 625 km, GUVI's far-ultraviolet (115 to 180 nm) scanning imaging spectrograph provided horizon-to-horizon images of the aurora. The width of single disk scan is 11.8 degrees.

Figure 3 shows an example comparison. In the upper left corner, Figure 3a shows the simulated electron flux. The time of this plot was chosen to be near the middle of the satellite pass, indicated both by the diagonal time stamp as well as the vertical black line in Figure 3c. Figure 3b shows GUVI data for 15:48 UT during the August 21st, 2002 storm. The starting position is indicated near dusk. Figure 3c shows the electron total energy flux averaged over the horizon to horizon swath width for the pass. The dashed black line indicates the GUVI swath averaged energy flux. The HEIDI electron flux was interpolated and averaged similarly for each time. The simulated aurora was slightly poleward of the measured aurora in the 21-03 MLT sector, but close to the same position in the 18-21 MLT sector. However, the strength of the aurora in the 18-21 MLT sector was smaller than the observations. This was a common theme among all of the comparisons, suggesting a shortcoming of the model in this region. A similar issue of the dusk side aurora was reported in *Chen et al.* [2015], likely due to a shortage of observations of very-low-frequency (VLF) waves by the SCATHA satellite, upon which the loss model was built [*Chen et al.*, 2005].

Programmatically determining the location of the diffuse aurora in both the data and model was difficult due to superposition of the discrete aurora and the presence of multiple auroral bands. To ensure an accurate comparison, each comparison between HEIDI and GUVI passes were analyzed by hand for all of the storm and τ_{max} combinations. The downside of the data model comparison using satellite data was that not every minute of model output could be compared. However, it was found that the location and strength of the HEIDI aurora did not vary significantly in the 20 or so minutes of a satellite pass. The only orbits considered were those where HEIDI was entirely in self-consistent mode. More specifically, the comparison was only done when the self-consistently calculated hemispheric power was greater than 10 GW. The analysis was further constrained to the northern hemisphere, since the electrodynamics were solved only in this hemisphere.

The location and strength of the diffuse aurora was compared in 3 hour MLT sectors, starting from 00 MLT. Discrete auroral arcs were not separately accounted for and comparisons were only recorded in MLT bins where GUVI data existed for more than 50% of the region. The process was defined as follows:

- Define the location of the HEIDI and GUVI aurora as the center of the auroral band with the most total energy flux
- Interpolate the simulated total energy flux to the locations of the GUVI measurements, averaged over times within ±15 seconds of the model output.
- Define the strength of the HEIDI and GUVI aurora as the average of the total energy flux in each MLT bin

Figure 3 was recreated for each storm, each simulation, and each satellite pass. For each of these, the location of the aurora was recorded from plots like Figures 3a and 3b in each MLT sector where GUVI data was available. Furthermore, the modeled and observed strengths in each sector with GUVI data were recorded. In total, over 600 comparisons were made, the results of which are shown in Figure 4.

Figure 4 quantifies the ability of the models with different τ_{max} values to capture gross features in the auroral observations. The coloring of each sector is the average difference between the total electron flux in HEIDI and GUVI. The yellow dots are the average location of the aurora in each MLT sector. The black lines, dashed for GUVI, are spline interpolations between the points to create a semi-realistic auroral oval to make comparisons easier. In plot A, the τ_{max} = 2 hour simulation results were dropped in the 15-18 sector because there were no times with GUVI observations where the model produced an aurora in that sector for this value of τ_{max}.

The location of the aurora in all four simulation sets shared a similar feature. The difference between the oval locations was very little in the 18-00 MLT sectors, but then increased more and more towards the dayside. This suggests that as electrons drifted towards dawn, they moved too far towards the Earth before being scattering at lower L-shells, and thus lower latitudes. The locations of the auroral ovals of the HEIDI simulations were nearly identical for the 4 hour, 8 hour, and energy dependent cases. The two hour case was vastly different, owing to the fact that 2 hours was not enough time for the electrons to drift as far as 09 MLT. A promising result was the 2 hour case from 09-15 MLT, where the location matched much better than the other cases.

The effects of the lifetimes are perhaps more visible in the strength results which are indicated by the colors in Figure 4. When compared with the τ_{max} = 8 hour runs in plot C, the τ_{max} = 2 runs in plot A had a stronger aurora in the 21-03 MLT sectors, but weaker in the 03-18 MLT region. Looking at the 21-00 MLT sector, the τ_{max} = 2 hour case over-predicted the strength of the aurora by 0.4 ergs cm^{-2} s^{-1}, but the τ_{max} = 8 case under-predicted by 1.4 ergs cm^{-2} s^{-1}. On the other side of the planet, in the 09-12 MLT sector, the results were flipped, with the τ_{max} = 2 case under-predicting by 0.9 ergs cm^{-2} s^{-1} and the τ_{max} = 8 case being nearly equal to the GUVI observations. The differences in the τ_{max} = 4 case were a meld between the τ_{max} = 2 and τ_{max} =

8, as expected. It is interesting that the latitude of the HEIDI aurora is unchanged in plots B-D. This suggests that the conductance changes resulting from this aurora were not enough to significantly alter the convection electric field. If that were the case, the extent to which electrons penetrate to lower L-shells would have been dependent on τ_{max}. The energy dependent case is unique in that the electron flux is greater than the other simulations on the entire nightside, from 18-06 MLT, but despite this some of the lower energy particles still circumnavigated the planet well past magnetic noon.

There are a couple important points to take away from this analysis. The first is that the pitch angle diffusion time limit greatly influenced the strength of the aurora in all MLT sectors. The second is that it only appears to have changed the location of the aurora in the $\tau_{max} = 2$ hour case. It should be noted that the results presented here are an average of all 4 storms, and that the response of each individual storm is quite different, as was demonstrated in the Dst^* results in Section 4.1. Conductance and electric potential results for individual storms are presented in Section 4.4, and Section 4.5 investigates what difference the conductance made on the ability of the model to reproduce realistic self-consistent electric fields.

4.3. Hemispheric Power

The hemispheric power (HP) is the total area integrated particle energy deposited into a hemisphere [*Fuller-Rowell and Evans*, 1987]. This quantity provides an initial large-scale metric for the amount of aurora produced by the model. Figure 5 shows a data-model comparison of HP for each storm and simulation in the northern hemisphere.

The HP for storm A matched reasonably well with observations, with all simulations tracking the approximate running average of the POES data for the majority of the storm time. Notice that the maximum diffusion lifetime near the beginning and end of the simulation had no effect on the HP at all. This is an indication that the auroral oval was outside of the HEIDI boundary during these times, and that the Ovation aurora was being used here. A curious result of the simulations in plot A is that the 4 hour τ_{max} produced more hemispheric power than the others for the first half of the storm. This is likely related to the energy dependent nature of the HP itself. As particles drift towards the Earth, they gain energy adiabatically due to the increasing magnetic field strength. In this case, the amount of electron flux diffusing into the loss cone was balanced by this energy enhancement. With a minimum Dst^* of -106 nT and maximum observed hemispheric power of just over 100 GW, the relative weakness of this storm suggests slower convection in the inner magnetosphere. As a result, the electrons move towards the Earth more slowly, and are more likely to be lost at a lower characteristic energy, resulting in less HP. The 4 hour τ_{max} simulation kept electrons around long enough for their energy to increase, but not too long as to prohibit their loss, as seen in the green line of the 8 hour simulation during the middle of the simulation. This conclusion is further supported by the energy dependent τ_{max}. Since the lower energy electrons were lost more slowly in this case, the fact the blue line HP was smaller for much of the storm suggests that the characteristic energies of the electrons were indeed low for this storm.

A more expected result comes from storm B. The POES HP was vastly overestimated by the model in this case, but the large response helped to exaggerate the τ_{max} differences. There are two important features to notice here. The first is that the shorter lifetimes produced significantly more aurora at the beginning of the storm. Around noon of August 18th, the $\tau_{max} = 2$ hour simulation produced 500 GW, but the $\tau_{max} = 8$ hour simulation produced only 200 GW, since electrons were allowed to persist longer in the latter case. The second feature to notice is the time shift of the response. The $\tau_{max} = 8$ hour simulation peaked 2 hours later than the $\tau_{max} = 2$ hour simulation, and was 120 GW less.

Figure 5c shows a case where the model under-predicted observations. There was little difference in magnitude between these simulations, but the timing of auroral enhancements were still shifted from each other albeit by time frames of under an hour. There are two factors that explain why HEIDI underestimated the HP in Figure 5c, but overestimated it in Figure 5b. The first is the outer boundary condition where electron flux observations were greater at geosynchronous orbit for storm 2. The second is the adiabatic heating of the electrons as they move closer to Earth. The electrons reached lower L-shells in Figure 5b, causing the energy and subsequent HP to increase. This was most likely driven by stronger convection electric fields for storm B.

Figure 5d is a good example of how shorter maximum lifetimes could produce more aurora initially, but less later. The $\tau_{max} = 2$ hour simulation had 100 GW more at its peak than the 8 hour simulation, but 30 GW less 12 hours later. All of the simulations in this case came close to the right values in addition to capturing the timings of HP increase well. These results suggest that the maximum diffusion lifetime had consequences on both the magnitude and timing of auroral enhancements produced by the model, but they were inconsistent between storms.

4.4. Conductance and Potentials

The conductivity and its gradients produced by the aurora are a primary factor in controlling the ionospheric electrodynamics in terms of ring current coupling [*Nopper and Carovillano*, 1978; *Vasyliunas*, 1970]. As equation 1 suggests, the average energy and electron flux of the aurora are essential to the description of the conductivity and therefore the height integrated conductance. This section highlights the differences in the time evolution in the conductances for each τ_{max}, and explores how that influenced the electric fields that drive plasma in the ionosphere-magnetosphere feedback system. For this analysis, the focus was on the August 18th, 2003 storm because the differences between simulations was greatest.

The auroral electron energy fluxes during four different times during the main phase of the storm are displayed in Figure 6. There were large differences between the different simulations (columns) at each time during the storm (rows). In the top row, early in the main phase, the aurora gained strength from the higher to lower τ_{max}. This is because during the beginning of the storm, few electrons had time to reach the maximum lifetime of the higher τ_{max} values, so they did not precipitate into the atmosphere. As the storm progressed, the simulations with a higher τ_{max} had much more wrapping of the aurora around towards the dayside. This was caused by the ability of longer lifetime electrons to $\mathbf{E} \times \mathbf{B}$ drift and gradient curvature drift towards the dawn and noon sectors. Complementary to this was a weaker aurora on the nightside for those cases. Since electrons drift towards the Earth across the entire nightside, there are large differences from about 21 MLT to the dawnside.

Figure 7 shows the Pedersen conductance for the same times and simulations as the energy flux results from Figure 6. The Pedersen conductance was calculated using the energy flux and average energy of precipitating electrons as described in Section 2, as well as a dayside driven conductance described by *Moen and Brekke* [1993]. While there were some regions where the auroral Pedersen conductance was stronger than the dayside conductance, the conductance produced by photoionization is generally larger than conductance from the aurora. In addition, because of the summer conditions where the dayside solar EUV dominated the conductance pattern, weaker electric fields and stronger field aligned currents would be expected [*Cnossen and Richmond*, 2012; *Cnossen and Förster*, 2016], as well as weaker responses to geomagnetic storms [*A et al.*, 2012; *Perlongo and Ridley*, 2016]. Since all of the storms chosen for this study were during the northern hemisphere summer, the amount of electrons making it beyond 06 MLT had little effect on the total Pedersen conductance on the dayside in any of the different simulations. In fact, there were almost no differences between simulations from 12-18 MLT.

An assumption of the Robinson formula is that the electron precipitation is Maxwellian in form, causing a peak in Pedersen conductance at an average energy of 4 keV, assuming a constant energy flux. As such, the conductances in Figure 7 don't necessarily correspond to the largest energy fluxes in Figure 6. This can particularly be seen at 9:14 UT in the $\tau_{max} = 4$ simulation, where the energy flux is greater towards dawn, but the conductance is largest towards dusk. In addition to this, the scattering rate, λ_ϕ, in equation 3 is dependent on the electron energy, MLT, and L-shell [*Chen et al.*, 2005]. Consequently, the average energy of the precipitating particles changed significantly between τ_{max} values. In the energy dependent case, higher average energies in the magnetospheric electrons resulted in shorter electron lifetimes, leading to a similar response as the $\tau_{max} = 2$ hour simulation. Throughout the storm, the larger nightside energy fluxes in the 2 hour case produced more Pedersen conductance there. In general, the conductance on the dawn side was significantly larger for the $\tau_{max} = 2$ hour case.

Figure 8 shows the total electric field strength for the same times as Figures 6 and 7. The black dashed line represents the boundary between the self-consistent calculations and the Weimer potentials, which are not shown, since they are the same in all τ cases. The electric fields on the dayside were relatively unchanged between the different simulations since the dayside total conductances were very similar to each other. Vastly different structures were seen on the nightside though, which were dependent on the scattering rate. In the τ_{max} = 8 and 4 hour simulations, a strong and narrow electric field, associated with a sub-auroral polarization stream (SAPS), developed in the 19-24 MLT region equatorward of the main auroral oval, but poleward of a detached auroral feature from 09:14 UT to 10:04 UT. This feature is highlighted in Figure 9, which shows the SAPS as well as the electron flux and Pedersen conductance for the τ_{max} = 8 hour case at 9:14 UT. The conductance was greater than 10 mhos at the center of the main auroral band in the region just poleward of the SAPS. Equatorward of that was a narrow band of less than 5 mho conductance. Further equatorward was an increase in Pedersen conductance to ~9 mho. This structure tended to confine the strong electric field channel to the narrow band between the primary and secondary conductance peaks. When this secondary peak did not exist, such as in the τ_{max} = 2 hour simulation case, a SAPS channel did not appear, but a penetration electric field extended much further equatorward. This is consistent with modeling efforts which have shown that an increase in ionospheric conductance reduces the shielding and therefore results in further inward transport of the ring current plasma and a stronger ring current [*Ebihara et al.*, 2004; *Zheng et al.*, 2008]. Figures 8-9 demonstrate that τ_{max} had a significant impact on the structure of the conductance patterns, which lead to major changes in the electric fields.

Figure 10 quantifies these results by averaging the ionospheric electric field strength, Pedersen conductivity, and FAC both in time and longitudinally. The left column shows each variable versus magnetic latitude averaged over 18-21 MLT. The right column is the same, but for 21-03 MLT. An average was then taken over all times during August 18th, 2003. These MLT regions were chosen because the electron scattering rates diverged mostly eastward of 21 MLT. Furthermore, most electric field plots showed SAPS developing in the 18-21 MLT region in the $\tau_{max} = 8$ and 4 hour simulations.

The electric fields for 18-21 MLT in Figure 10a show the high latitude electric field decreasing towards lower magnetic latitudes until about 54°, where there was an enhancement in the $\tau_{max} = 8$ and 4 hour simulations. In this region the Pedersen conductance in Figure 10c was generally low, so these electric fields can be attributed to SAPS. There was little difference in this region in conductance due to the characteristics of the electron scattering model used, except that the 2 hour case was slightly higher. The electric field was 2.1 mV/m less in this case compared to the average of the other simulations.

The behavior of the FAC current in Figure 10e also varied for each τ_{max}. This was expected since each τ_{max} drives different conductances, which leads to different electric fields, which then map back to the ring current, changing the convection electric field which drives the ion convection. This then changes the azimuthal pressure gradients in the ring current, which drive FACs. Since so many processes occur between the conductance differences from the electron scattering rates and the FAC changes near the end of the feedback loop, it is impossible to draw causal relationships from this. However, treating the rest of the ring current like a black box, the FAC plots do demonstrate that changes of just 10% in the ionospheric electric fields can alter the position and magnitude of subsequent FAC by at least 50%, as was the case between the energy dependent and τ_{max} = 8 and 2 hour simulations in Figure 10f. Furthermore, the location of the peak of the FAC in Figure 10e moved 3 degrees equatorward when the electric field was an average of 2.8 mV/m less in the 2 hour verses the energy dependent simulation, but this shift was not seen in the other simulations where the electric field was also decreased.

The Pedersen conductance in the 21-03 MLT region in Figure 10d were much more stratified than the dusk results in Figure 10c. This is congruent with the auroral locations presented in Section 4.2 for all storms: The 2 hour simulation had the most conductance, followed by the energy dependent, 4 hour, and 8 hour simulations. The two simulations with the larger conductances had higher electric fields within the auroral zone, while Equation 2 implies that lower conductivity leads to higher electric field[s], these averages show that a higher total conductance in a region can lead to larger electric fields in the same general area. The FAC equatorward of the strong electric field shows these two simulations as having the largest FAC's also, which may contribute to the strong electric fields, despite the strong conductance. The strong electric fields may further be a result of the structure in the aurora. When the aurora is enhanced among multiple bands created by the energy dependence in the loss model, it is more likely that strong electric fields will develop around them, as seen in Figure 8. Figure 10b shows that the electric field can vary from 21-03 MLT between 16 mV/m and 22 mV/m between the 4 hour and energy dependent simulations at 60°. In other words, the auroral zone experienced a 26% larger electric field when averaged over the entire storm in these longitudes. This demonstrates how significant the effects of changing the maximum lifetime of electrons in the ring current has in self-consistent M-I models.

A major shortcoming of the model at this time is the amount of smoothing that is needed to be done for numerical stability given the resolution of the model. It is expected that this smoothing produces artificially small electric fields due to the flattened conductance gradients. Furthermore, any small-scale structures in electron precipitation or the subsequent electrodynamics are indiscernible. The effects of these limitations are explored further in section 4.5, but first the simulations are compared to different data sets.

4.5. Ionospheric Electric Fields

Data from the Defense Meteorological Satellites Program (DMSP) [*Hardy*, 1984; *Rich and Hairston*, 1994; *Hairston et al.*, 1998] was used to compare the modeled electric field results for each storm. Unfortunately, a full MLT analysis like in Section 4.2 could not be performed because there were not enough times when GUVI observations overlapped DMSP satellite tracks. The lack of discrete aurora in the model further complicated such an analysis since it was not possible to discern electric fields resulting from conductance produced by discrete or diffuse aurora. For these reasons, only a couple examples are shown in Figures 11 and 12 to demonstrate the model's electric field results.

Figure 11 demonstrates a time during the August 21st, 2002 storm when the GUVI observations matched very well in both strength and magnitude near 20 MLT, where DMSP took measurements. While the magnitude of the velocity in Figure 10e matched relatively well with a root-mean-square-error (RMSE) of about 200 m/s, the small scale structure of the aurora seen in red was completely missed. This was unsurprising since the resolution of the electrodynamics model was 2.8° in longitude and 1.8° in latitude. Furthermore, the smoothing done to merge with the Weimer potentials poleward of the boundary made it difficult, if not impossible, to model small-scale electric fields properly here. Small-scale electric fields associated with discrete aurora are also missing from the model at this time. Figure 12 shows a time where HEIDI completely missed a large auroral enhancement. DMSP observed velocities over 2000 m/s both equatorward and poleward of the auroral oval, while HEIDI predicted a maximum velocity of just 420 m/s on the poleward side. Furthermore, the velocity was much slower for the entire flyby of the 18-21 MLT region.

The point of these figures is primarily to show how important the scattering rate, and subsequent conductances can be to accurately capturing the overall strength of the electric fields in the ionosphere. They also show that when the auroral strength and location matches observations, the model does reasonably capture the gross electric field strength.

In the future, data providing boundary conditions for much more recent storms will become available and allow the model to be run and compared with data from a plethora of electric field measurements, including the Super Dual Auroral Radar Network (Super-DARN) [*Greenwald et al.*, 1995], and incoherent scatter radars; as well as auroral imagery from the SSUSI instrument on DMSP.

5. Discussion and Summary

In recent years, there has been a push for magnetosphere-ionosphere-thermosphere models to become fully coupled and self-consistent. This study advanced one link in that chain by creating a version of HEIDI that computes both electric fields and auroral precipitation self-consistently with auroral precipitation. This is an updated version of HEIDI. In the previous version, the aurora was quite idealized, and was driven by a simple relationship with the FACs [*Ridley and Liemohn*, 2002; *Liemohn et al.*, 2004]. The new version of the model used a much more complex description of the aurora and compared better to Dst^*

than HEIDI with a Volland-Stern electric field [*Volland*, 1973; *Stern*, 1975], but comparisons between observation and model results of aurora and ionospheric electric fields varied greatly. The hemispheric power plots and aggregate analysis of the HEIDI and GUVI aurora demonstrate the importance of running models for a wide variety of events and parameters, the maximum diffusive scattering lifetime in this case.

This study imposed an upper limit on the electron scattering rates defined by the *Chen et al.* [2005] loss model, which was found to produce exceedingly long lifetimes at low L-shells [*Chen et al.*, 2015]. This parameter, τ_{max}, was shown to have significant impacts on the strength and location of the simulated aurora, as well as the electrodynamic system. It was found that a limit of $\tau_{max} = 2$ hours produced the best agreement with the location of the aurora observed by GUVI, but $\tau_{max} = 4$ hours agreed best with the total energy flux averaged over all sectors. In the $\tau_{max} = 2$ hours case, the strength of the aurora was increased in the 21-03 MLT sector, but fewer electrons drifted around the Earth and precipitated on the dayside, especially in the 09-12 MLT sector. The total energy flux produced by the different τ_{max} values were consistent with the idea that a smaller τ_{max} should produce more aurora on the nightside and less on the dayside.

Furthermore, average differences in ionospheric conductances of just a few mhos between τ_{max} simulations led to more than a 25% change in electric field strength in the 21-03 MLT region. While not shown systematically, it was observed that times when the aurora match observations, the electric fields in the ionosphere were on par with measurements from DMSP.

If τ_{max} had such a large effect on electric fields, then the $\mathbf{E} \times \mathbf{B}$ drift speeds of the electrons should have also differed between simulations. However, the location of the simulated aurora stayed relatively constant between the different τ_{max} values. This is evident in Figure 6 where the choice of τ_{max} altered the longitudinal extent of the energy flux to a much larger degree than in latitude. If the $\mathbf{E} \times \mathbf{B}$ drift speed were smaller for a particular τ_{max}, the electrons should have precipitated at larger L-shells and higher latitudes. While it appears this occurred for the $\tau_{max} = 2$ hour simulation in many of the MLT sectors of plot A in Figure 3, Figure 10 showed that it did not have a consistently smaller electric field than the other τ_{max} values in the 21-03 MLT sector. Since this is the sector where the strength of the aurora differed the most from the $\tau_{max} = 4$ and $\tau_{max} = 8$ simulations, this mechanism does not explain the improvement in auroral locations on the nightside or dayside of the $\tau_{max} = 2$ hour simulation. It also indicates that the large scale convection electric field was not greatly influenced by τ_{max}. Furthermore, changes in the convection electric field brought on by the inclusion of ionospheric electrodynamics are responsible for altering the rate of the ion outflow through the dayside magnetopause, a process determined to be the primary loss mechanism for the ions in this model [*Liemohn et al.*, 1999]. If the outflow rate of the ions was altered between τ_{max} simulations, there would have been greater difference in Dst^*.

Another way that τ_{max} could effect the location of the diffuse aurora is by changing the characteristic energy of the electron population that reach a given MLT sector. Higher energy particles will gradient-curvature drift at larger L-shells and thus precipitate at higher latitudes. τ_{max} also puts a limit on the distance that cold plasma can gradient-curvature drift before being lost to the thermosphere. The higher latitude dayside aurora in the $\tau_{max} = 2$ hours case could result from these two factors. The cold electrons were lost before they were able to drift past 09 MLT, but the higher energy electrons persisted at larger L-shells until 15 MLT. Despite the better match for $\tau_{max} = 2$ hours, HEIDI produced an aurora 5-10° equatorward of the GUVI observations for all τ_{max} from 00 to 12 MLT, perhaps due to the relatively close outer-boundary of geosynchronous orbit, or lower plasma average energies than reality. Further research should be done to identify if this is a common bias in the HEIDI model and, if so, determine the cause of it.

The choice in τ_{max} was shown to alter the simulation's ability to reproduce auroral features by a large degree. While the arbitrarily chosen $\tau_{max} = 2$ hour simulation matched the location of the aurora the best, all of the simulations presented here demonstrate the importance of understanding the electron loss rates in the ring current. Since small deviations in the upper limit of the scattering rates were shown to have a large effect on the electrodynamic results, any uncertainty in this parameter is a major hindrance to the accuracy of M-I coupled models. This offers a cautionary tale in ring current modeling. Moving from more empirically driven models to self-consistent frameworks adds complexity that could make the results less predictive until each parameter is modeled accurately. For example, running HEIDI in self-consistent mode puts significantly more pressure on the electron scattering model to be correct because of the electrodynamic feedback loop. As a result, times when the scattering diverges from observations may result in a much worse off solution than empirical versions. Transitioning to self-consistent models should therefore be done keeping the assumptions and errors of all components between models in mind.

References

A, E., A. J. Ridley, D. Zhang, and Z. Xiao (2012), Analyzing the hemispheric asymmetry in the thermospheric density response to geomagnetic storms, *Journal of Geophysical Research*, *117*(A8), A08,317, doi:10.1029/2011JA017259.

Albert, J. M. (1994), Quasi-linear pitch angle diffusion coefficients: Retaining high harmonics, *Journal of Geophysical Research*, *99*(A12), 23,741, doi:10.1029/94JA02345.

Belian, R. D., G. R. Gisler, T. Cayton, and R. Christensen (1992), High- <i>Z</i> energetic particles at geosynchronous orbit during the Great Solar Proton Event Series of October 1989, *Journal of Geophysical Research*, *97*(A11), 16,897, doi:10.1029/92JA01139.

Belmont, G., D. Fontaine, and P. Canu (1983), Are equatorial electron cyclotron waves responsible for diffuse auroral electron precipitation?, *Journal of Geophysical Research: Space Physics*, *88*(A11), 9163–9170, doi:10.1029/JA088iA11p09163.

Burke, W. J. (2007), Penetration electric fields: A VollandStern approach, *Journal of Atmospheric and Solar-Terrestrial Physics*, *69*(10-11), 1114–1126, doi: 10.1016/j.jastp.2006.09.013.

Chen, M. W., and M. Schulz (2001), Simulations of diffuse aurora with plasma sheet electrons in pitch angle diffusion less than everywhere strong, *Journal of Geophysical Research: Space Physics*, *106*(A12), 28,949–28,966, doi:10.1029/2001JA000138.

Chen, M. W., M. Schulz, G. Lu, and L. R. Lyons (2003), Quasi-steady drift paths in a model magnetosphere with AMIE electric field: Implications for ring current formation, *Journal of Geophysical Research: Space Physics*, *108*(A5), doi:10.1029/2002JA009584.

Chen, M. W., M. Schulz, P. C. Anderson, G. Lu, G. Germany, and M. Wüest (2005), Storm time distributions of diffuse auroral electron energy and X-ray flux: Comparison of drift-loss simulations with observations, *Journal of Geophysical Research*, *110*(A3), A03,210, doi:10.1029/2004JA010725.

Chen, M. W., C. L. Lemon, T. B. Guild, A. M. Keesee, A. Lui, J. Goldstein, J. V. Rodriguez, and P. C. Anderson (2015), Effects of modeled ionospheric conductance and electron loss on self-consistent ring current simulations during the 5-7 April 2010 storm, *Journal of Geophysical Research: Space Physics*, *120*(7), 5355–5376, doi: 10.1002/2015JA021285.

Christensen, A. B. (2003), Initial observations with the Global Ultraviolet Imager (GUVI) in the NASA TIMED satellite mission, *Journal of Geophysical Research*, *108*(A12), 1451, doi:10.1029/2003JA009918.

Cnossen, I., and M. Förster (2016), North-ncessouth asymmetries in the polar thermosphere-ionosphere system: Solar cycle and seasonal influe, *Journal of Geophysical Research: Space Physics*, *121*(1), 612–627, doi:10.1002/2015JA021750.

Cnossen, I., and A. D. Richmond (2012), How changes in the tilt angle of the geomagnetic dipole affect the coupled magnetosphere-ionosphere-thermosphere system, *Journal of Geophysical Research*, *117*(A10), A10,317, doi:10.1029/2012JA018056.

Daglis, I., G. Balasis, N. Ganushkina, F.-A. Metallinou, M. Palmroth, R. Pirjola, and I. Tsagouri (2009), Investigating dynamic coupling in geospace through the combined use of modeling, simulations and data analysis, *Acta Geophysica*, *57*(1), doi: 10.2478/s11600-008-0055-5.

Deng, W., T. L. Killeen, A. G. Burns, and R. G. Roble (1991), The flywheel effect: Ionospheric currents after a geomagnetic storm, *Geophysical Research Letters*, *18*(10), 1845–1848, doi:10.1029/91GL02081.

Dessler, A. J., and E. N. Parker (1959), Hydromagnetic theory of geomagnetic storms, *Journal of Geophysical Research*, *64*(12), 2239–2252, doi:10.1029/JZ064i012p02239.

Ebihara, Y., and M. Ejiri (1998), Modeling of solar wind control of the ring current buildup: A case study of the magnetic storms in April 1997, *Geophysical Research Letters*, *25*(20), 3751–3754, doi:10.1029/1998GL900006.

Ebihara, Y., and M. Ejiri (2000), Simulation study on fundamental properties of the storm-time ring current, *Journal of Geophysical Research: Space Physics*, *105*(A7), 15,843–15,859, doi:10.1029/1999JA900493.

Ebihara, Y., M. Fok, R. A. Wolf, T. J. Immel, and T. E. Moore (2004), Influence of ionosphere conductivity on the ring current, *Journal of Geophysical Research*, *109*(A8), A08,205, doi:10.1029/2003JA010351.

Fok, M.-C., and T. E. Moore (1997), Ring current modeling in a realistic magnetic field configuration, *Geophysical Research Letters*, *24*(14), 1775–1778, doi:10.1029/97GL01255.

Fok, M.-C., R. A. Wolf, R. W. Spiro, and T. E. Moore (2001), Comprehensive computational model of Earth's ring current, *Journal of Geophysical Research: Space Physics*, *106*(A5), 8417–8424, doi:10.1029/2000JA000235.

Fok, M.-C., A. Glocer, Q. Zheng, R. Horne, N. Meredith, J. Albert, and T. Nagai (2011), Recent developments in the radiation belt environment model, *Journal of Atmospheric and Solar-Terrestrial Physics*, *73*(11), 1435–1443, doi:10.1016/j.jastp.2010.09.033.

Fok, M.-C., N. Y. Buzulukova, S.-H. Chen, A. Glocer, T. Nagai, P. Valek, and J. D. Perez (2014), The Comprehensive Inner Magnetosphere-Ionosphere Model, *Journal of Geophysical Research: Space Physics*, *119*(9), 7522–7540, doi:10.1002/2014JA020239.

Frank, L. A. (1967), On the extraterrestrial ring current during geomagnetic storms, *Journal of Geophysical Research*, *72*(15), 3753–3767, doi:10.1029/JZ072i015p03753.

Fuller-Rowell, T. J., and D. S. Evans (1987), Height-integrated Pedersen and Hall conductivity patterns inferred from the TIROS-NOAA satellite data, *Journal of Geophysical Research*, *92*(A7), 7606, doi:10.1029/JA092iA07p07606.

Galand, M., and A. D. Richmond (2001), Ionospheric electrical conductances produced by auroral proton precipitation, *Journal of Geophysical Research: Space Physics*, *106*(A1), 117–125, doi:10.1029/1999JA002001.

Gannon, J., and J. Love (2011), USGS 1-min Dst index, *Journal of Atmospheric and Solar-Terrestrial Physics*, *73*(2-3), 323–334, doi:10.1016/j.jastp.2010.02.013.

Garner, T., G. Crowley, and R. Wolf (2007), The impact of stormtime changes in the non-auroral conductance upon the low- and mid-latitude electric field, *Journal of Atmospheric and Solar-Terrestrial Physics*, *69*(10), 1200–1212, doi:10.1016/j.jastp.2006.09.010.

Gough, M. P., P. J. Christiansen, G. Martelli, and E. J. Gershuny (1979), Interaction of electrostatic waves with warm electrons at the geomagnetic equator, *Nature*, *279*(5713), 515–517, doi:10.1038/279515a0.

Greenwald, R. A., K. B. Baker, J. R. Dudeney, M. Pinnock, T. B. Jones, E. C. Thomas, J. P. Villain, J. C. Cerisier, C. Senior, C. Hanuise, R. D. Hunsucker, G. Sofko, J. Koehler, E. Nielsen, R. Pellinen, A. D. M. Walker, N. Sato, and H. Yamagishi (1995), DARN/SuperDARN, *Space Science Reviews*, *71*(1-4), 761–796, doi:10.1007/BF00751350.

Gu, X., Y. Y. Shprits, and B. Ni (2012), Parameterized lifetime of radiation belt electrons interacting with lower-band and upper-band oblique chorus waves, *Geophysical Research Letters*, *39*(15), doi:10.1029/2012GL052519.

Hairston, M. R., R. A. Heelis, and F. J. Rich (1998), Analysis of the ionospheric cross polar cap potential drop using DMSP data during the National Space Weather Program study period, *Journal of Geophysical Research: Space Physics*, *103*(A11), 26,337–26,347, doi:10.1029/97JA03241.

Hardy, D. A. (1984), Precipitating electron and ion detectors (SSJ/4) for the block 5D/flights 6-10 DMSP satellites: calibration and data presentation, *Rep. AFGL-TR-84-0317*.

Huang, C., S. Sazykin, and J. Goldstein (2007), Storm-time penetration electric fields and their effects: Magnetospheric and ionospheric perspectives, *Journal of Atmospheric and Solar-Terrestrial Physics*, *69*(10-11), 1111–1113, doi:10.1016/j.jastp.2007.03.005.

Ilie, R., M. W. Liemohn, G. Toth, and R. M. Skoug (2012), Kinetic model of the inner magnetosphere with arbitrary magnetic field, *Journal of Geophysical Research: Space Physics*, *117*(A4), n/a–n/a, doi:10.1029/2011JA017189.

Ilie, R., M. W. Liemohn, G. Toth, N. Yu Ganushkina, and L. K. S. Daldorff (2015), Assessing the role of oxygen on ring current formation and evolution through numerical experiments, *Journal of Geophysical Research: Space Physics*, *120*(6), 4656–4668, doi:10.1002/2015JA021157.

Jordanova, V. K. (2003), Ring current asymmetry from global simulations using a high-resolution electric field model, *Journal of Geophysical Research*, *108*(A12), 1443, doi:10.1029/2003JA009993.

Jordanova, V. K., and Y. Miyoshi (2005), Relativistic model of ring current and radiation belt ions and electrons: Initial results, *Geophysical Research Letters*, *32*(14), n/a–n/a, doi:10.1029/2005GL023020.

Jordanova, V. K., J. Albert, and Y. Miyoshi (2008), Relativistic electron precipitation by EMIC waves from self-consistent global simulations, *Journal of Geophysical Research: Space Physics*, *113*(A3), n/a–n/a, doi:10.1029/2008JA013239.

Jordanova, V. K., Y. Yu, J. T. Niehof, R. M. Skoug, G. D. Reeves, C. A. Kletzing, J. F. Fennell, and H. E. Spence (2014), Simulations of inner magnetosphere dynamics with an expanded RAM-SCB model and comparisons with Van Allen Probes observations, *Geophysical Research Letters*, *41*(8), 2687–2694, doi:10.1002/2014GL059533.

Kaeppler, S. R., D. L. Hampton, M. J. Nicolls, A. Strømme, S. C. Solomon, J. H. Hecht, and M. G. Conde (2015), An investigation comparing ground-based techniques that quantify auroral electron flux and conductance, *Journal of Geophysical Research: Space Physics*, *120*(10), 9038–9056, doi:10.1002/2015JA021396.

Katus, R. M., M. W. Liemohn, E. L. Ionides, R. Ilie, D. Welling, and L. K. Sarno-Smith (2015), Statistical analysis of the geomagnetic response to different solar wind drivers and the dependence on storm intensity, *Journal of Geophysical Research: Space Physics*, *120*(1), 310–327, doi:10.1002/2014JA020712.

Kennel, C. F. (1969), Consequences of a magnetospheric plasma, *Reviews of Geophysics*, *7*(1, 2), 379, doi:10.1029/RG007i001p00379.

Khazanov, G. V., M. W. Liemohn, T. S. Newman, M. Fok, and R. W. Spiro (2003), Self-consistent magnetosphere-ionosphere coupling: Theoretical studies, *Journal of Geophysical Research*, *108*(A3), 1122, doi:10.1029/2002JA009624.

Kozyra, J. U., M.-C. Fok, E. R. Sanchez, D. S. Evans, D. C. Hamilton, and A. F. Nagy (1998), The role of precipitation losses in producing the rapid early recovery phase of the Great Magnetic Storm of February 1986, *Journal of Geophysical Research*, *103*(A4), 6801, doi:10.1029/97JA03330.

Kozyra, J. U., M. W. Liemohn, C. R. Clauer, A. J. Ridley, M. F. Thomsen, J. E. Borovsky, J. L. Roeder, V. K. Jordanova, and W. D. Gonzalez (2002), Multistep Dst development and ring current composition changes during the 4-6 June 1991 magnetic storm, *Journal of Geophysical Research: Space Physics*, *107*(A8), SMP 33–1–SMP 33–22, doi:10.1029/2001JA000023.

Kronberg, E. A., M. Ashour-Abdalla, I. Dandouras, D. C. Delcourt, E. E. Grigorenko, L. M. Kistler, I. V. Kuzichev, J. Liao, R. Maggiolo, H. V. Malova, K. G. Orlova, V. Peroomian, D. R. Shklyar, Y. Y. Shprits, D. T. Welling, and L. M. Zelenyi (2014), Circulation of Heavy Ions and Their Dynamical Effects in the Magnetosphere: Recent Observations and Models, *Space Science Reviews*, *184*(1-4), 173–235, doi:10.1007/s11214-014-0104-0.

Lemon, C., R. A. Wolf, T. W. Hill, S. Sazykin, R. W. Spiro, F. R. Toffoletto, J. Birn, and M. Hesse (2004), Magnetic storm ring current injection modeled with the Rice Convection Model and a self-consistent magnetic field, *Geophysical Research Letters*, *31*(21), n/a–n/a, doi:10.1029/2004GL020914.

Liemohn, M. W., J. U. Kozyra, V. K. Jordanova, G. V. Khazanov, M. F. Thomsen, and T. E. Cayton (1999), Analysis of early phase ring current recovery mechanisms during geomagnetic storms, *Geophysical Research Letters*, *26*(18), 2845–2848, doi:10.1029/1999GL900611.

Liemohn, M. W., J. U. Kozyra, M. F. Thomsen, J. L. Roeder, G. Lu, J. E. Borovsky, and T. E. Cayton (2001a), Dominant role of the asymmetric ring current in producing the stormtime Dst *, *Journal of Geophysical Research*, *106*(A6), 10,883, doi: 10.1029/2000JA000326.

Liemohn, M. W., J. U. Kozyra, C. R. Clauer, and A. J. Ridley (2001b), Computational analysis of the near-Earth magnetospheric current system during two-phase decay storms, *Journal of Geophysical Research*, *106*(A12), 29,531, doi:10.1029/2001JA000045.

Liemohn, M. W., A. J. Ridley, D. L. Gallagher, D. M. Ober, and J. U. Kozyra (2004), Dependence of plasmaspheric morphology on the electric field description during the recovery phase of the 17 April 2002 magnetic storm, *Journal of Geophysical Research*, *109*(A3), A03,209, doi:10.1029/2003JA010304.

Liemohn, M. W., A. J. Ridley, P. C. Brandt, D. L. Gallagher, J. U. Kozyra, D. M. Ober, D. G. Mitchell, E. C. Roelof, and R. DeMajistre (2005), Parametric analysis of nightside conductance effects on inner magnetospheric dynamics for the 17 April 2002 storm, *Journal of Geophysical Research*, *110*(A12), A12S22, doi:10.1029/2005JA011109.

Liemohn, M. W., A. J. Ridley, J. U. Kozyra, D. L. Gallagher, M. F. Thomsen, M. G. Henderson, M. H. Denton, P. C. Brandt, and J. Goldstein (2006), Analyzing electric field morphology through data-model comparisons of the Geospace Environment Modeling Inner Magnetosphere/Storm Assessment Challenge events, *Journal of Geophysical Research*, *111*(A11), A11S11, doi:10.1029/2006JA011700.

Liemohn, M. W., M. Jazowski, J. U. Kozyra, N. Ganushkina, M. F. Thomsen, and J. E. Borovsky (2010), CIR versus CME drivers of the ring current during intense magnetic storms, *Proceedings of the Royal Society A: Mathematical, Physical and Engineering*

Sciences, *466*(2123), 3305–3328, doi:10.1098/rspa.2010.0075.

Liu, S., M. W. Chen, J. L. Roeder, L. R. Lyons, and M. Schulz (2005), Relative contribution of electrons to the stormtime total ring current energy content, *Geophysical Research Letters*, *32*(3), L03,110, doi:10.1029/2004GL021672.

Love, J. J., and J. L. Gannon (2009), Revised <I>D_{st}</I> and the epicycles of magnetic disturbance: 19582007, *Annales Geophysicae*, *27*(8), 3101–3131, doi:10.5194/angeo-27-3101-2009.

Lyons, L. R., R. M. Thorne, and C. F. Kennel (1972), Pitch-angle diffusion of radiation belt electrons within the plasmasphere, *Journal of Geophysical Research*, *77*(19), 3455–3474, doi:10.1029/JA077i019p03455.

McComas, D. J., S. J. Bame, B. L. Barraclough, J. R. Donart, R. C. Elphic, J. T. Gosling, M. B. Moldwin, K. R. Moore, and M. F. Thomsen (1993), Magnetospheric plasma analyzer: Initial three-spacecraft observations from geosynchronous orbit, *Journal of Geophysical Research: Space Physics*, *98*(A8), 13,453–13,465, doi:10.1029/93JA00726.

McComas, ., . Bame, . Barker, . Feldman, . Phillips, . Riley, and . Griffee (1998), Solar Wind Electron Proton Alpha Monitor (SWEPAM) for the Advanced Composition Explorer, *Space Science Reviews*, (1), 563–612, doi:10.1023/A:1005040232597.

Meredith, N. P., A. D. Johnstone, S. Szita, R. B. Horne, and R. R. Anderson (1999), Pancake electron distributions in the outer radiation belts, *Journal of Geophysical Research: Space Physics*, *104*(A6), 12,431–12,444, doi:10.1029/1998JA900083.

Meredith, N. P., R. B. Horne, A. D. Johnstone, and R. R. Anderson (2000), The temporal evolution of electron distributions and associated wave activity following substorm injections in the inner magnetosphere, *Journal of Geophysical Research: Space Physics*, *105*(A6), 12,907–12,917, doi:10.1029/2000JA900010.

Meredith, N. P., R. B. Horne, R. M. Thorne, D. Summers, and R. R. Anderson (2004), Substorm dependence of plasmaspheric hiss, *Journal of Geophysical Research*, *109*(A6), A06,209, doi:10.1029/2004JA010387.

Mitchell, E. J., P. T. Newell, J. W. Gjerloev, and K. Liou (2013), OVATION-SM: A model of auroral precipitation based on SuperMAG generalized auroral electrojet and substorm onset times, *Journal of Geophysical Research: Space Physics*, *118*(6), 3747–3759, doi:10.1002/jgra.50343.

Miyoshi, Y. S., V. K. Jordanova, A. Morioka, M. F. Thomsen, G. D. Reeves, D. S. Evans, and J. C. Green (2006), Observations and modeling of energetic electron dynamics during the October 2001 storm, *Journal of Geophysical Research*, *111*(A11), A11S02, doi:10.1029/2005JA011351.

Moen, J., and A. Brekke (1993), The solar flux influence on quiet time conductances in the auroral ionosphere, *Geophysical Research Letters*, *20*(10), 971–974, doi: 10.1029/92GL02109.

Moldwin, M. B., L. Downward, H. K. Rassoul, R. Amin, and R. R. Anderson (2002), A new model of the location of the plasmapause: CRRES results, *Journal of Geophysical Research*, *107*(A11), 1339, doi:10.1029/2001JA009211.

Newell, P. T., and J. W. Gjerloev (2011), Evaluation of SuperMAG auroral electrojet indices as indicators of substorms and auroral power, *Journal of Geophysical Research*, *116*(A12), A12,211, doi:10.1029/2011JA016779.

Ni, B., R. M. Thorne, R. B. Horne, N. P. Meredith, Y. Y. Shprits, L. Chen, and W. Li (2011a), Resonant scattering of plasma sheet electrons leading to diffuse auroral precipitation: 1. Evaluation for electrostatic electron cyclotron harmonic waves, *Journal of Geophysical Research: Space Physics*, *116*(A4), n/a–n/a, doi:10.1029/2010JA016232.

Ni, B., R. M. Thorne, N. P. Meredith, R. B. Horne, and Y. Y. Shprits (2011b), Resonant scattering of plasma sheet electrons leading to diffuse auroral precipitation: 2. Evaluation for whistler mode chorus waves, *Journal of Geophysical Research: Space Physics*, *116*(A4), n/a–n/a, doi:10.1029/2010JA016233.

Ni, B., J. Liang, R. M. Thorne, V. Angelopoulos, R. B. Horne, M. Kubyshkina, E. Spanswick, E. F. Donovan, and D. Lummerzheim (2012), Efficient diffuse auroral electron scattering by electrostatic electron cyclotron harmonic waves in the outer magnetosphere: A detailed case study, *Journal of Geophysical Research: Space Physics*, *117*(A1), n/a–n/a, doi:10.1029/2011JA017095.

Nopper, R. W., and R. L. Carovillano (1978), Polar-equatorial coupling during magnetically active periods, *Geophysical Research Letters*, *5*(8), 699–702, doi: 10.1029/GL005i008p00699.

Orlova, K., and Y. Shprits (2014), Model of lifetimes of the outer radiation belt electrons in a realistic magnetic field using realistic chorus wave parameters, *Journal of Geophysical Research: Space Physics*, *119*(2), 770–780, doi:10.1002/2013JA019596.

Orlova, K., Y. Shprits, and M. Spasojevic (2016), New global loss model of energetic and relativistic electrons based on Van Allen Probes measurements, *Journal of Geophysical Research: Space Physics*, *121*(2), 1308–1314, doi:10.1002/2015JA021878.

Paxton, L. J., A. B. Christensen, D. C. Humm, B. S. Ogorzalek, C. T. Pardoe, D. Morrison, M. B. Weiss, W. Crain, P. H. Lew, D. J. Mabry, J. O. Goldsten, S. A. Gary, D. F. Persons, M. J. Harold, E. B. Alvarez, C. J. Ercol, D. J. Strickland, and C.-I. Meng

(1999), <title>Global ultraviolet imager (GUVI): measuring composition and energy inputs for the NASA Thermosphere Ionosphere Mesosphere Energetics and Dynamics (TIMED) mission</title>, in *SPIE's International Symposium on Optical Science, Engineering, and Instrumentation*, edited by A. M. Larar, pp. 265–276, International Society for Optics and Photonics, doi:10.1117/12.366380.

Paxton, L. J., A. B. Christensen, D. Morrison, B. Wolven, H. Kil, Y. Zhang, B. S. Ogorzalek, D. C. Humm, J. O. Goldsten, R. DeMajistre, and C.-I. Meng (2004), <title>GUVI: a hyperspectral imager for geospace</title>, in *Fourth International Asia-Pacific Environmental Remote Sensing Symposium 2004: Remote Sensing of the Atmosphere, Ocean, Environment, and Space*, edited by C. A. Nardell, P. G. Lucey, J.-H. Yee, and J. B. Garvin, pp. 228–240, International Society for Optics and Photonics, doi: 10.1117/12.579171.

Perlongo, N. J., and A. J. Ridley (2016), Universal time effect in the response of the thermosphere to electric field changes, *Journal of Geophysical Research: Space Physics*, *121*(4), 3681–3698, doi:10.1002/2015JA021636.

Peymirat, C. (2002), Neutral wind influence on the electrodynamic coupling between the ionosphere and the magnetosphere, *Journal of Geophysical Research*, *107*(A1), 1006, doi:10.1029/2001JA900106.

Rich, F. J., and M. Hairston (1994), Large-scale convection patterns observed by DMSP, *Journal of Geophysical Research*, *99*(A3), 3827, doi:10.1029/93JA03296.

Ridley, A., Y. Deng, and G. Tóth (2006), The global ionospherethermosphere model, *Journal of Atmospheric and Solar-Terrestrial Physics*, *68*(8), 839–864, doi: 10.1016/j.jastp.2006.01.008.

Ridley, A. J., and M. W. Liemohn (2002), A model-derived storm time asymmetric ring current driven electric field description, *Journal of Geophysical Research: Space Physics*, *107*(A8), SMP 2–1–SMP 2–12, doi:10.1029/2001JA000051.

Ridley, A. J., T. I. Gombosi, and D. L. DeZeeuw (2004), Ionospheric control of the magnetosphere: conductance, *Annales Geophysicae*, *22*(2), 567–584, doi:10.5194/angeo-22-567-2004.

Robinson, R. M., R. R. Vondrak, K. Miller, T. Dabbs, and D. Hardy (1987), On calculating ionospheric conductances from the flux and energy of precipitating electrons, *Journal of Geophysical Research*, *92*(A3), 2565, doi:10.1029/JA092iA03p02565.

Roeder, J. L., and H. C. Koons (1989), A survey of electron cyclotron waves in the magnetosphere and the diffuse auroral electron precipitation, *Journal of Geophysical Research*, *94*(A3), 2529, doi:10.1029/JA094iA03p02529.

Schulz, M. (1974), Particle lifetimes in strong diffusion, *Astrophysics and Space Science*, *31*(1), 37–42, doi:10.1007/BF00642599.

Schumaker, T. L., M. S. Gussenhoven, D. A. Hardy, and R. L. Carovillano (1989), The relationship between diffuse auroral and plasma sheet electron distributions near local midnight, *Journal of Geophysical Research: Space Physics*, *94*(A8), 10,061–10,078, doi: 10.1029/JA094iA08p10061.

Sckopke, N. (1966), A general relation between the energy of trapped particles and the disturbance field near the Earth, *Journal of Geophysical Research*, *71*(13), 3125–3130, doi:10.1029/JZ071i013p03125.

Shprits, Y. Y., S. R. Elkington, N. P. Meredith, and D. A. Subbotin (2008a), Review of modeling of losses and sources of relativistic electrons in the outer radiation belt I:

Radial transport, *Journal of Atmospheric and Solar-Terrestrial Physics*, *70*(14), 1679–1693, doi:10.1016/j.jastp.2008.06.008.

Shprits, Y. Y., D. A. Subbotin, N. P. Meredith, and S. R. Elkington (2008b), Review of modeling of losses and sources of relativistic electrons in the outer radiation belt II: Local acceleration and loss, *Journal of Atmospheric and Solar-Terrestrial Physics*, *70*(14), 1694–1713, doi:10.1016/j.jastp.2008.06.014.

Smith, ., . L'Heureux, . Ness, . Acuña, . Burlaga, and . Scheifele (1998), The ACE Magnetic Fields Experiment, *Space Science Reviews*, (1), 613–632, doi:10.1023/A:1005092216668.

Stern, D. P. (1975), The motion of a proton in the equatorial magnetosphere, *Journal of Geophysical Research*, *80*(4), 595–599, doi:10.1029/JA080i004p00595.

Sugiura, M., T. Kamei, A. Berthelier, and M. Menvielle (1991), Equatorial Dst Index: 1957-1986.

Thorne, R. M., B. Ni, X. Tao, R. B. Horne, and N. P. Meredith (2010), Scattering by chorus waves as the dominant cause of diffuse auroral precipitation., *Nature*, *467*(7318), 943–6, doi:10.1038/nature09467.

Toffoletto, F., S. Sazykin, R. Spiro, and R. Wolf (2003), Inner magnetospheric modeling with the Rice Convection Model, \ssr, *107*, 175–196, doi:10.1023/A:1025532008047.

Tóth, G., I. V. Sokolov, T. I. Gombosi, D. R. Chesney, C. R. Clauer, D. L. De Zeeuw, K. C. Hansen, K. J. Kane, W. B. Manchester, R. C. Oehmke, K. G. Powell, A. J. Ridley, I. I. Roussev, Q. F. Stout, O. Volberg, R. A. Wolf, S. Sazykin, A. Chan, B. Yu, and J. Kóta (2005), Space Weather Modeling Framework: A new tool for the space science community, *Journal of Geophysical Research*, *110*(A12), A12,226, doi:10.1029/2005JA011126.

Tóth, G., B. van der Holst, I. V. Sokolov, D. L. De Zeeuw, T. I. Gombosi, F. Fang, W. B. Manchester, X. Meng, D. Najib, K. G. Powell, Q. F. Stout, A. Glocer, Y.-J. Ma, and M. Opher (2012), Adaptive numerical algorithms in space weather modeling, *Journal of Computational Physics*, *231*(3), 870–903, doi:10.1016/j.jcp.2011.02.006.

Vasyliunas, V. M. (1970), Mathematical Models of Magnetospheric Convection and its Coupling to the Ionosphere, pp. 60–71, Springer Netherlands, doi:10.1007/978-94-010-3284-1$_6$.

Volland, H. (1973), A semiempirical model of large-scale magnetospheric electric fields, *Journal of Geophysical Research*, *78*(1), 171–180, 10.1029/JA078i001p00171.

Weimer, D. R. (1996), A flexible, IMF dependent model of high-latitude electric potentials having Space Weather applications, *Geophysical Research Letters*, *23*(18), 2549–2552, 10.1029/96GL02255.

Weimer, D. R. (2001), An improved model of ionospheric electric potentials including substorm perturbations and application to the Geospace Environment Modeling November 24, 1996, event, *Journal of Geophysical Research: Space Physics*, *106*(A1), 407–416, 10.1029/2000JA000604.

Weimer, D. R. (2005), Improved ionospheric electrodynamic models and application to calculating Joule heating rates, *Journal of Geophysical Research*, *110*(A5), A05,306, 10.1029/2004JA010884.

Welling, D. T., M. André, I. Dandouras, D. Delcourt, A. Fazakerley, D. Fontaine, J. Foster, R. Ilie, L. Kistler, J. H. Lee, M. W. Liemohn, J. A. Slavin, C.-P. Wang, M. Wiltberger, and A. Yau (2015a), The Earth: Plasma Sources, Losses, and Transport Processes, *Space Science Reviews*, *192*(1-4), 145–208, 10.1007/s11214-015-0187-2.

Welling, D. T., V. K. Jordanova, A. Glocer, G. Toth, M. W. Liemohn, and D. R. Weimer (2015b), The two-way relationship between ionospheric outflow and the ring current, *Journal of Geophysical Research: Space Physics*, *120*(6), 4338–4353, 10.1002/2015JA021231.

Winglee, R. M., D. Chua, M. Brittnacher, G. K. Parks, and G. Lu (2002), Global impact of ionospheric outflows on the dynamics of the magnetosphere and cross-polar cap potential, *Journal of Geophysical Research*, *107*(A9), 1237, 10.1029/2001JA000214.

Wolf, R., R. Spiro, G.-H. Voigt, P. Reiff, C.-K. Chen, and M. Harel (1982), Computer simulation of inner magnetospheric dynamics for the magnetic storm of July 29, 1977, *\jgr*, *87*, 5949–5962, 10.1029/JA087iA08p05949.

Wolf, R., R. Spiro, S. Sazykin, and F. Toffoletto (2007), How the Earth's inner magnetosphere works: An evolving picture, *Journal of Atmospheric and Solar-Terrestrial Physics*, *69*(3), 288–302, 10.1016/j.jastp.2006.07.026.

Young, D. T., H. Balsiger, and J. Geiss (1982), Correlations of magnetospheric ion composition with geomagnetic and solar activity, *Journal of Geophysical Research*, *87*(A11), 9077, 10.1029/JA087iA11p09077.

Yu, Y., and A. J. Ridley (2013), Exploring the influence of ionospheric O ⁺ outflow on magnetospheric dynamics: The effect of outflow intensity, *Journal of Geophysical Research: Space Physics*, *118*(9), 5522–5531, 10.1002/jgra.50528.

Yu, Y., V. K. Jordanova, A. J. Ridley, J. M. Albert, R. B. Horne, and C. A. Jeffery (2016), A new ionospheric electron precipitation module coupled with RAM-SCB within the geospace general circulation model, *Journal of Geophysical Research: Space Physics*, *121*(9), 8554–8575, 10.1002/2016JA022585.

Zaharia, S., V. K. Jordanova, M. F. Thomsen, and G. D. Reeves (2006), Self-consistent modeling of magnetic fields and plasmas in the inner magnetosphere: Application to a geomagnetic storm, *Journal of Geophysical Research*, *111*(A11), A11S14, 10.1029/2006JA011619.

Zaharia, S., V. K. Jordanova, D. Welling, and G. Tóth (2010), Self-consistent inner magnetosphere simulation driven by a global MHD model, *Journal of Geophysical Research: Space Physics*, *115*(A12), n/a–n/a, 10.1029/2010JA015915.

Zhang, J., I. G. Richardson, D. F. Webb, N. Gopalswamy, E. Huttunen, J. C. Kasper, N. V. Nitta, W. Poomvises, B. J. Thompson, C.-C. Wu, S. Yashiro, and A. N. Zhukov (2007), Solar and interplanetary sources of major geomagnetic storms (<i>Dst</i> 100 nT) during 1996-2005, *Journal of Geophysical Research: Space Physics*, *112*(A10), n/a–n/a, 10.1029/2007JA012321.

Zheng, Y., P. C. Brandt, A. T. Y. Lui, and M.-C. Fok (2008), On ionospheric trough conductance and subauroral polarization streams: Simulation results, *Journal of Geophysical Research*, *113*(A4), A04,209, 10.1029/2007JA012532.

Zou, S., M. B. Moldwin, A. J. Ridley, M. J. Nicolls, A. J. Coster, E. G. Thomas, and J. M. Ruohoniemi (2014), On the generation/decay of the storm-enhanced density plumes: Role of the convection flow and field-aligned ion flow, *Journal of Geophysical Research: Space Physics*, *119*(10), 8543–8559, 10.1002/2014JA020408.

Acknowledgments. This research was supposed by NSF through grants AGS-1010812 and ANT-0838828, and NASA grant NNG04GK18G. This work was made possible by NASA HEC Pleiades allocation. We would also like to acknowledge high-performance computing support from Yellowstone (ark:/85065/d7wd3xhc) provided by NCAR's Computational and Information Systems Laboratory, sponsored by the National Science Foundation. We would also like to thank the International Space Science Institute (ISSI) for supporting this collaborative effort. The DMSP and GUVI data used in this study can be obtained from JHU/APL. The simulation results are available upon request.

Table 1. Synopsis of geomagnetic storm events simulated.

#	Time (UT)	Dst	Type
1	2002/08/21 0700	-106	CME
2	2003/08/18 1600	-148	CME
3	2003/07/12 0600	-105	CIR
4	2005/08/31 1600	-131	CIR

fig1.png

Figure 1. Schematics of the new self-consistent aurora and one-way coupling between the ring current solver, HEIDI, and the ionosphere/thermosphere model, GITM

DST2.png

Figure 2. Dst* data-model comparison for all 4 storms and all simulations. The dashed black and purple lines show the Kyoto Dst* and USGS Dst* respectively. The dark grey line is the Volland-Stern run. The blue, green, red, and brown lines show the energy dependent, 8 hour, 4 hour, and 2 hour τ_{max} runs.

GUVI1.jpg

Figure 3. This snapshot compares the HEIDI electron flux in plot A to the GUVI observed aurora in plot B for the August 21st, 2002 storm with a τ_{max} of 2 hours. The dashed black line in plot C shows 30 second bins of the average GUVI electron flux per swath. The solid green line are the HEIDI values interpolated to those times and regions. The vertical black bar in plot C is the time at which plot A is drawn.

dial.jpg

Figure 4. Comparison of the strength and location of the aurora between HEIDI and GUVI for each τ_{max} for all storms and times. The colors represent the average difference between HEIDI and GUVI in each sector, blue meaning HEIDI was smaller, red meaning larger. The yellow dots are the average location of the aurora. These are connected by solid black lines for HEIDI and dashed black lines for GUVI. These lines were created with spline interpolations.

HP2.png

Figure 5. Hemispheric power comparison for all 4 storms and τ_{max} values. The dashed black lines are the observations derived from NOAA POES satellites measurements. The blue, green, red, and brown lines show the energy dependent, 8 hour, 4 hour, and 2 hour τ_{max} runs. Times when all the colored lines are on top of each other indicate when only Ovation SME was used to specify the aurora.

eflux_new.png

Figure 6. Energy fluxes in $erg/cm^2/s$ for each τ_{max} during the August 18th, 2003 storm. Each row is a different time during the main phase of the storm. The first column is for a $\tau_{max} = 8$ hours , the second for $\tau_{max} = 4$ hours, the third for $\tau_{max} = 2$ hours, and the fourth for the energy dependent τ_{max}. Each subfigure is plotted in magnetic coordinates, with 12 MLT at the top. The bounding magnetic latitude is 50°. The hemispheric power is shown in the bottom right of each subplot.

sigmaP.png

Figure 7. Total Pedersen conductance, including solar and auroral sources for each τ_{max} during the August 18th, 2003 storm in the same format as Figure 6.

EFIELD.png

Figure 8. Total electric field magnitude for each τ_{max} during the August 18th, 2003 storm. The dashed line represents the outer boundary of HEIDI. Poleward of this boundary the potentials were described by the Weimer electric potential model.

saps.png

Figure 9. Expanded electric field (A), electron flux (B), and Pedersen conductance (C) plots from August 18th, 2003 at 9:14 UT. All 3 plots are from the $\tau_{max} = 8$ hour simulation case. The red circle highlights the SAPS feature.

line_efield.png

Figure 10. The electric field strength, Pedersen conductivity, and FAC for each τ_{max} in the top, middle, and bottom rows respectively. Each parameter is averaged over 18-21 MLT in the left column and 21-03 MLT in the right column. The results are further averaged over all times during the main phase of the August 18th, 2003 storm.

figure_11.png

Figure 11. (A) the HEIDI electric potentials, (B) electron flux, and (C) Pedersen conductivity during the August 21st, 2002 storm for a $\tau_{max} = 2$ hours. (D) the GUVI auroral observations. The over-plotted black lines are the DMSP orbit paths. (E) The dashed black line is the cross track plasma velocity of DMSP at the HEIDI 1 min output interval; the green line is the equivalent V_y for HEIDI interpolated to the DMSP location; and the dark grey shaded region indicates poleward of the 67° HEIDI boundary. The red line is the high resolution raw DMSP data.

figure_12.png

Figure 12. The same as Figure 11, but for a τ_{max} of 8 hours during the August 18th, 2003 storm.

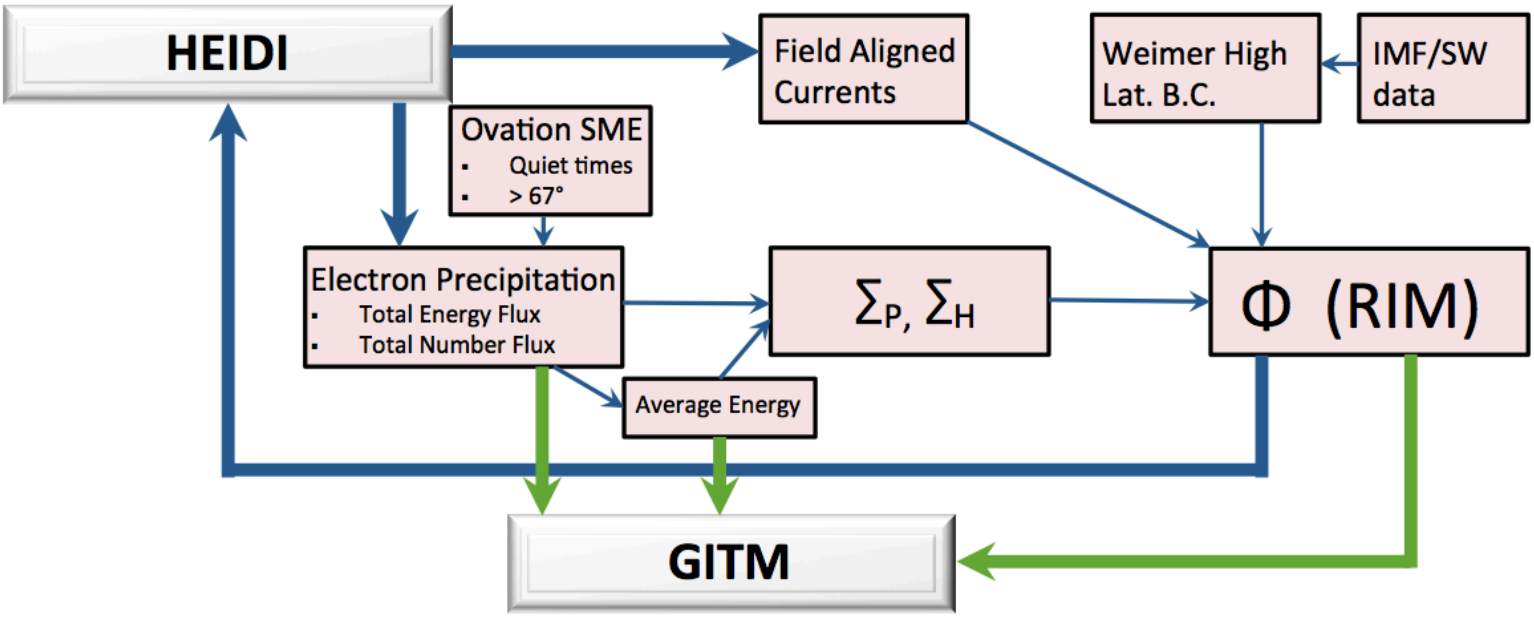

2016JA023679-f01-z-.png

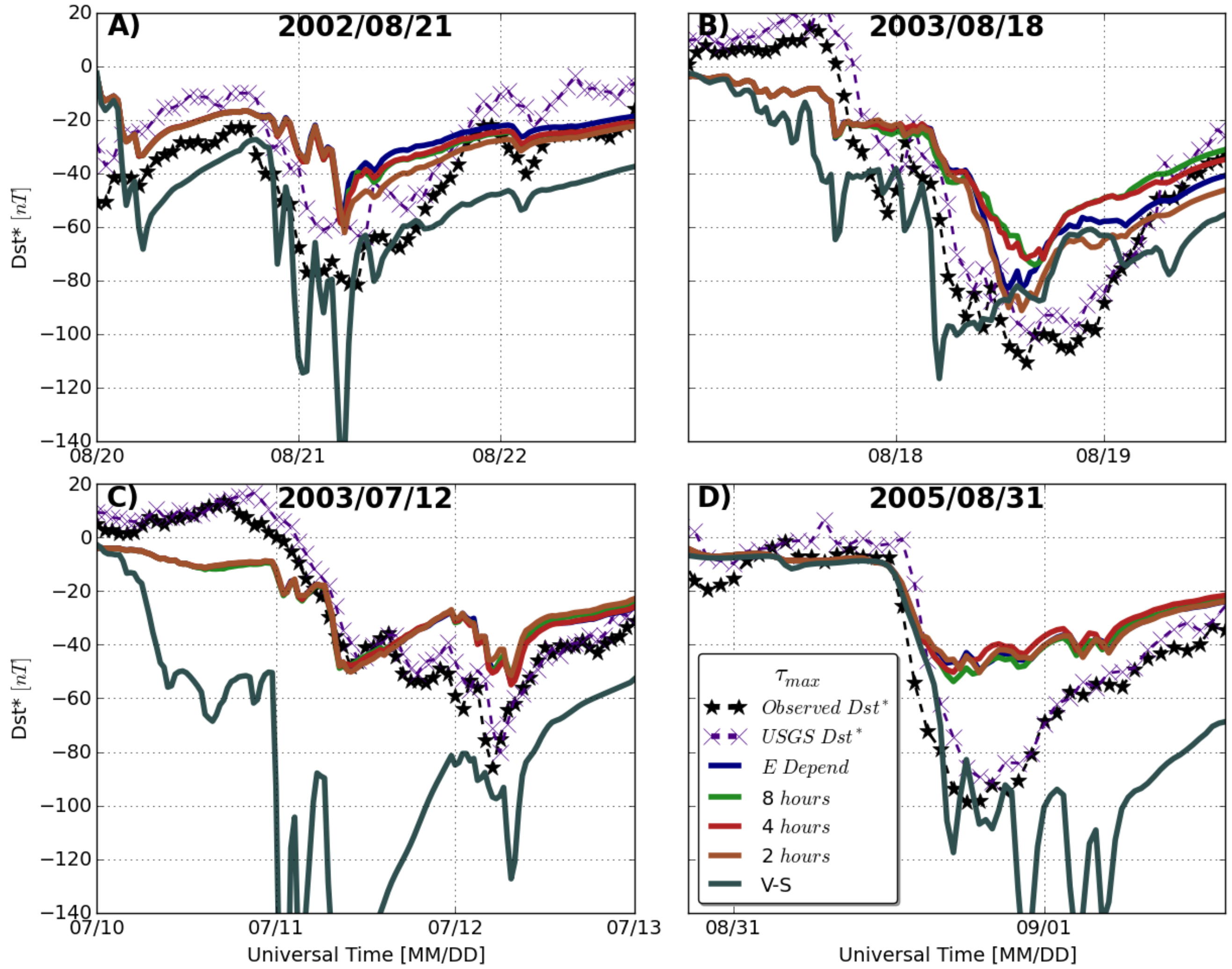

2016JA023679-f02-z-.png

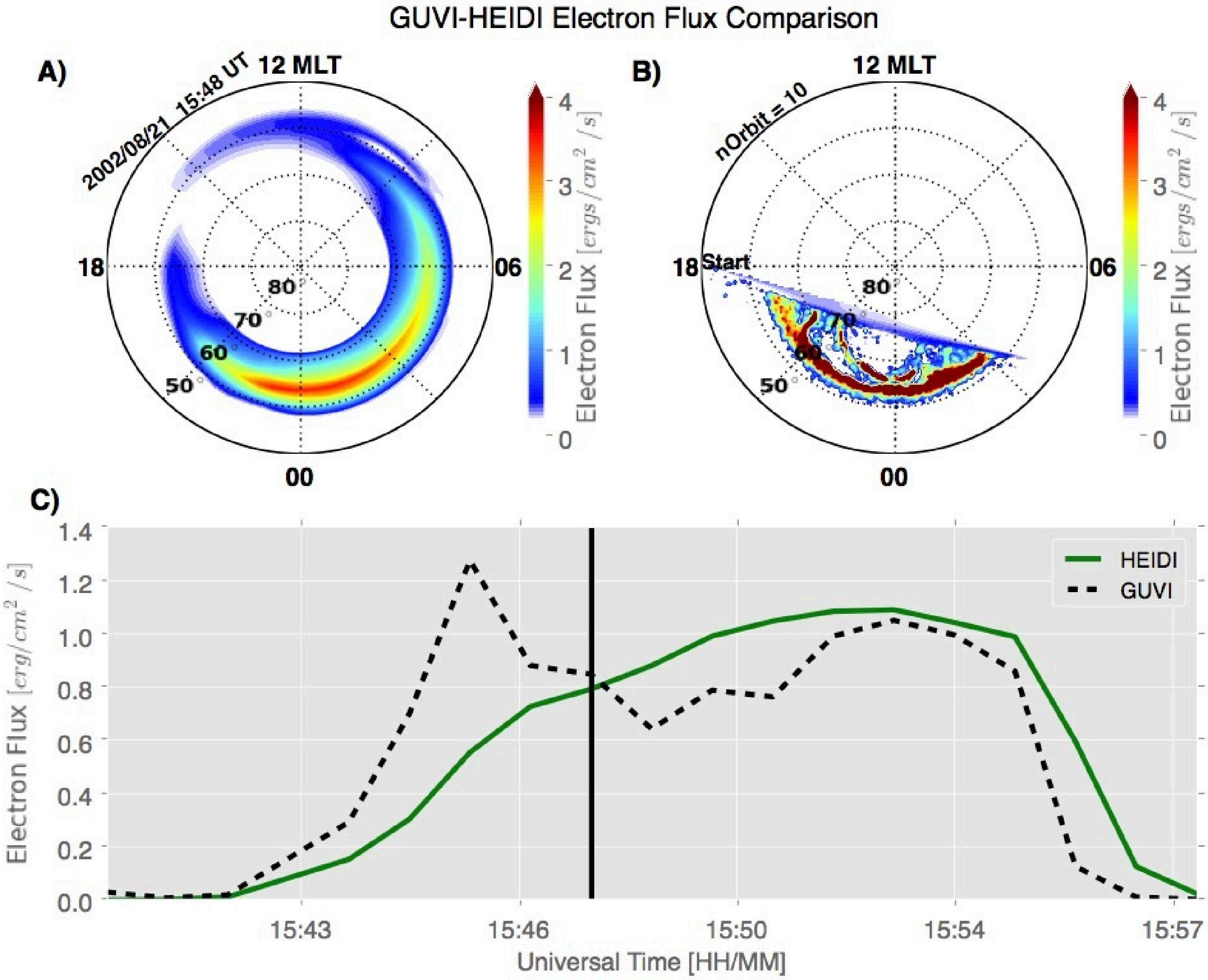

2016JA023679-f03-z-.jpg

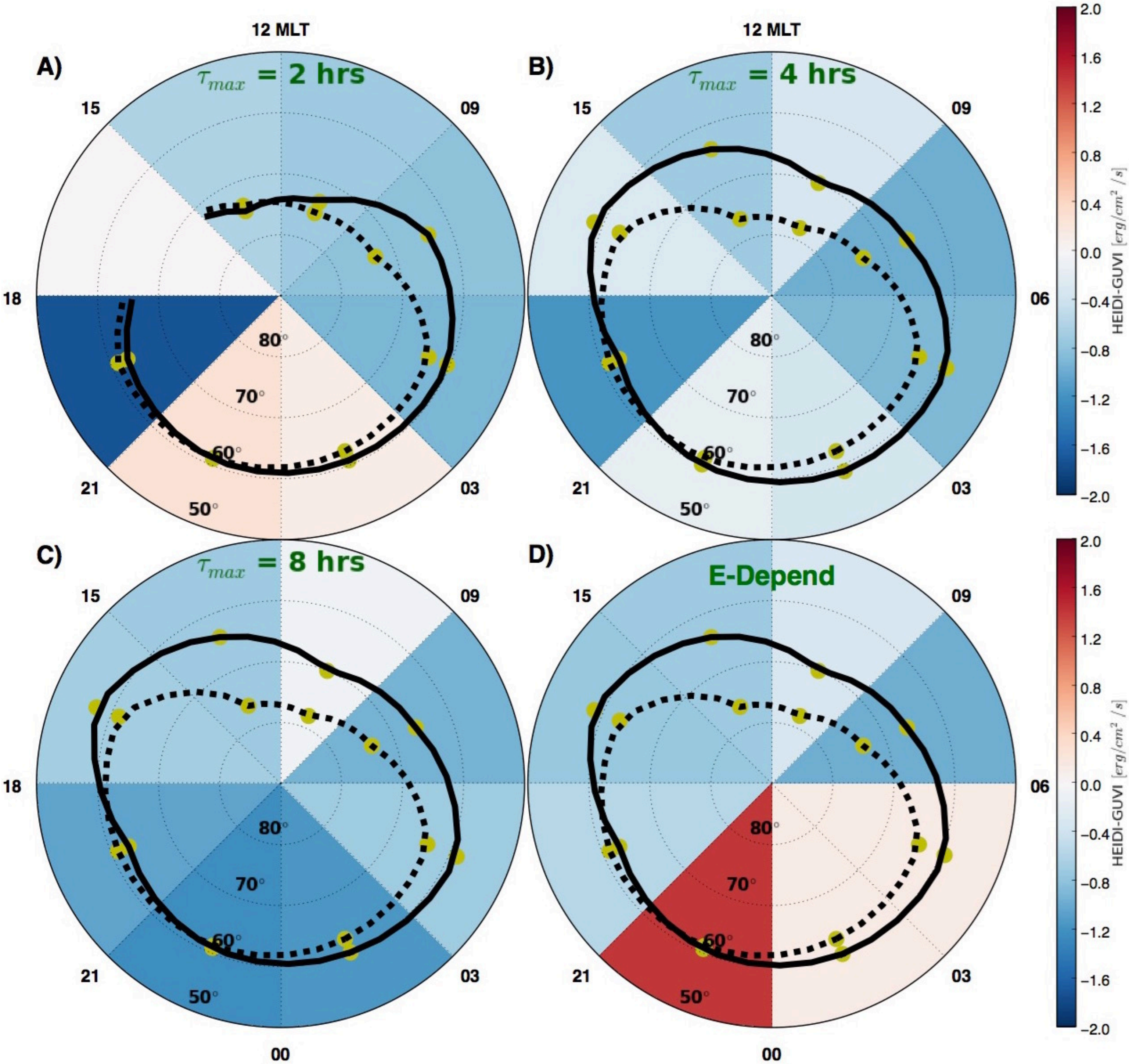

2016JA023679-f04-z-.jpg

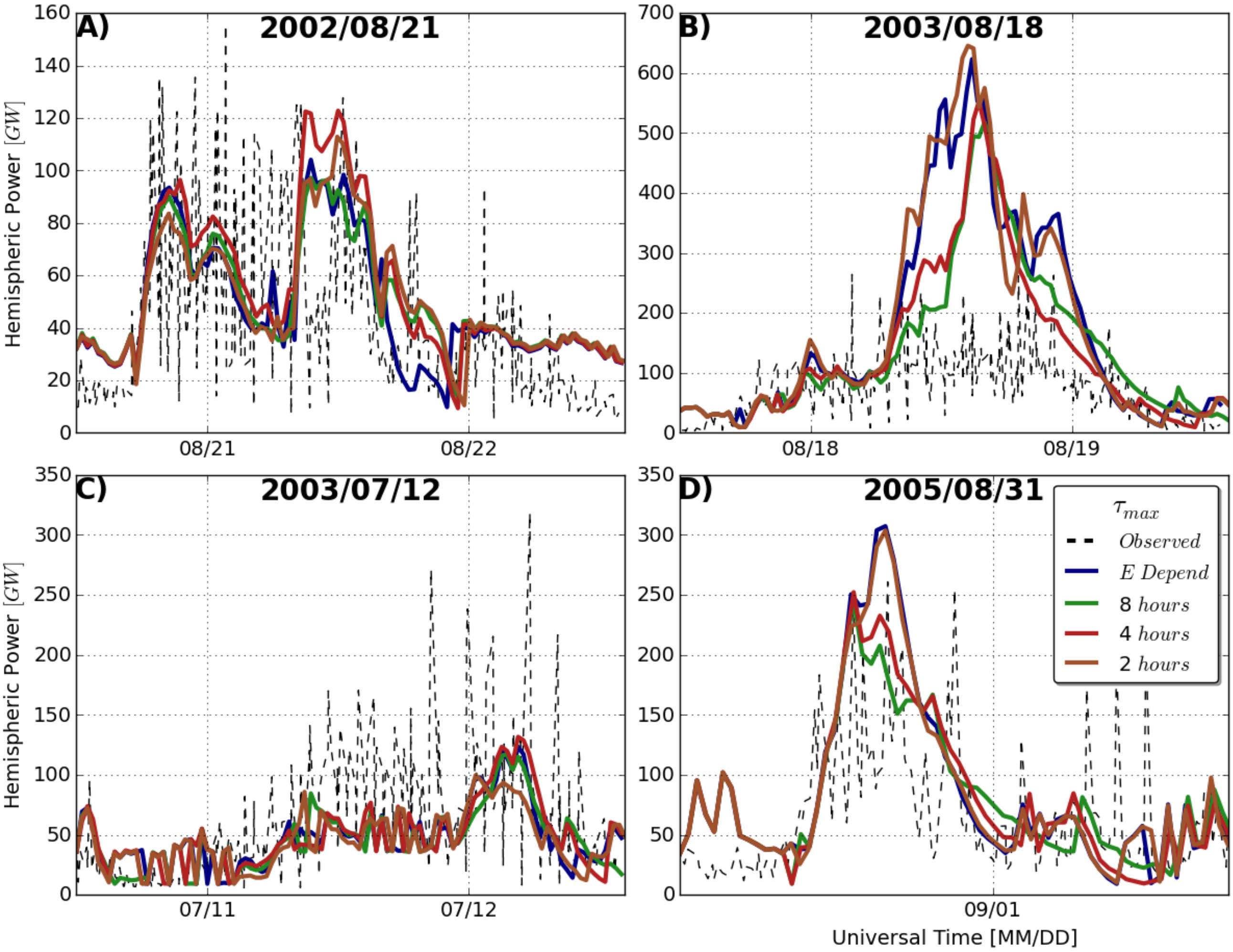

2016JA023679-f05-z-.png

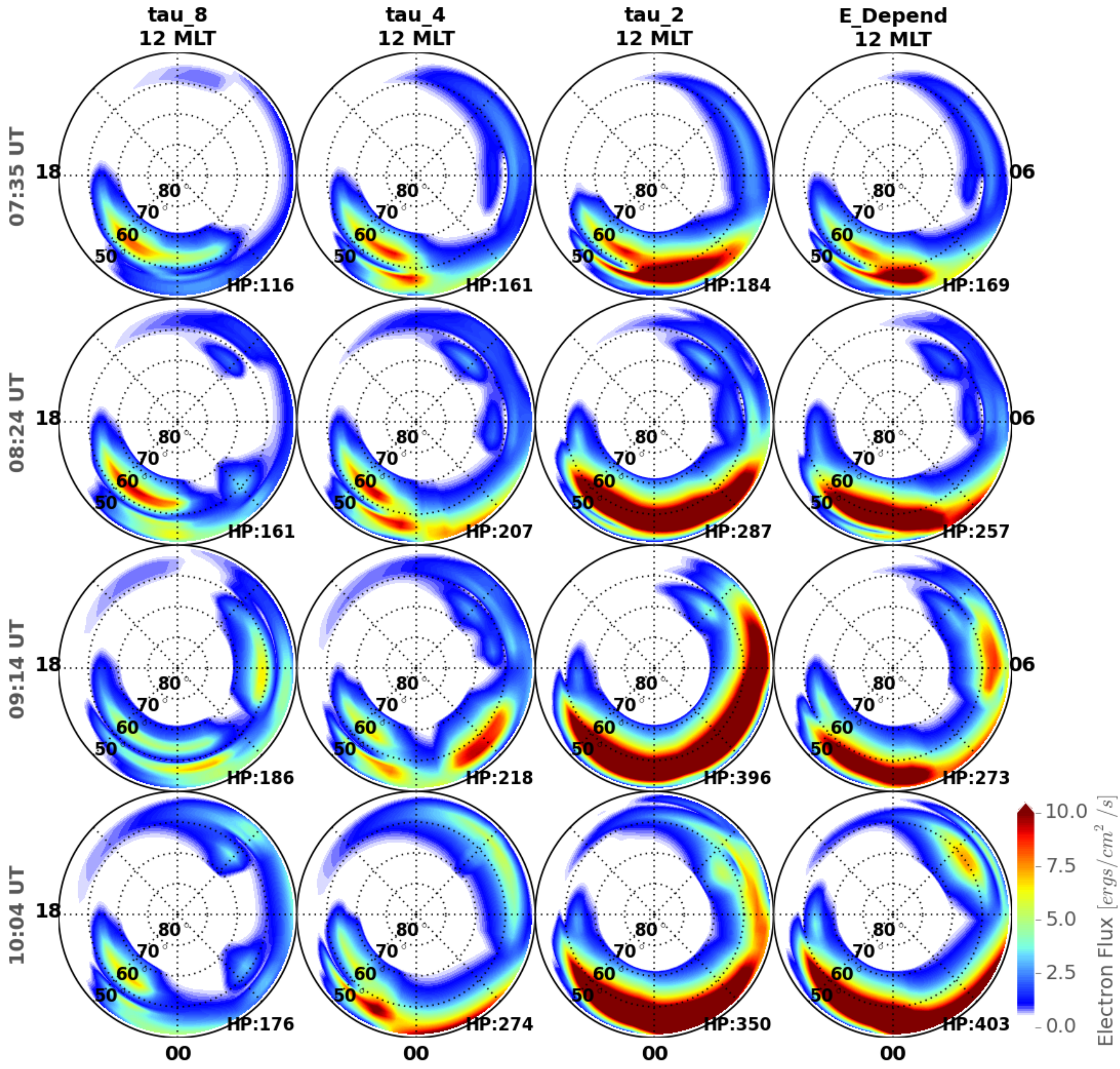

2016JA023679-f06-z-.png

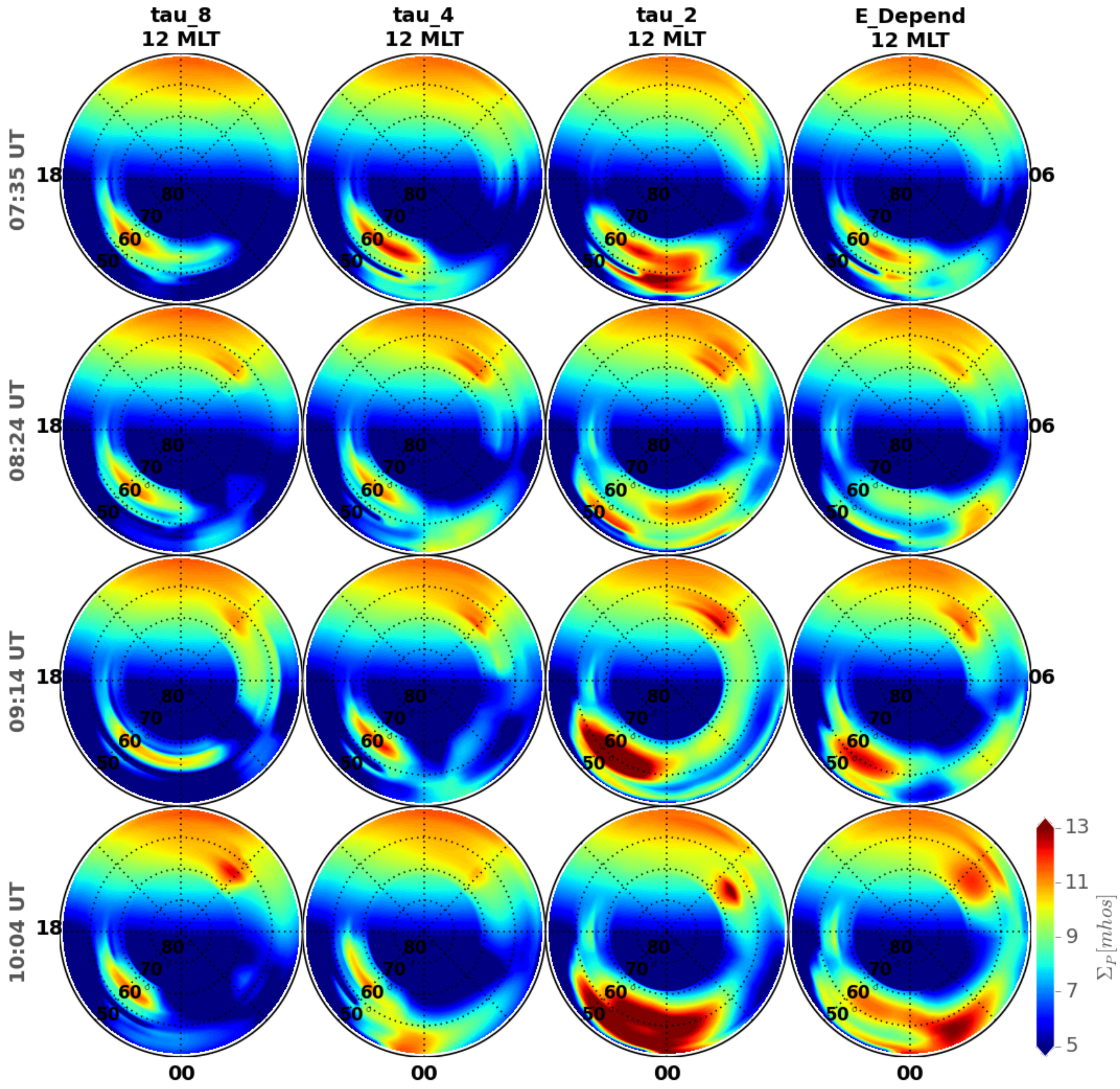

2016JA023679-f07-z-.png

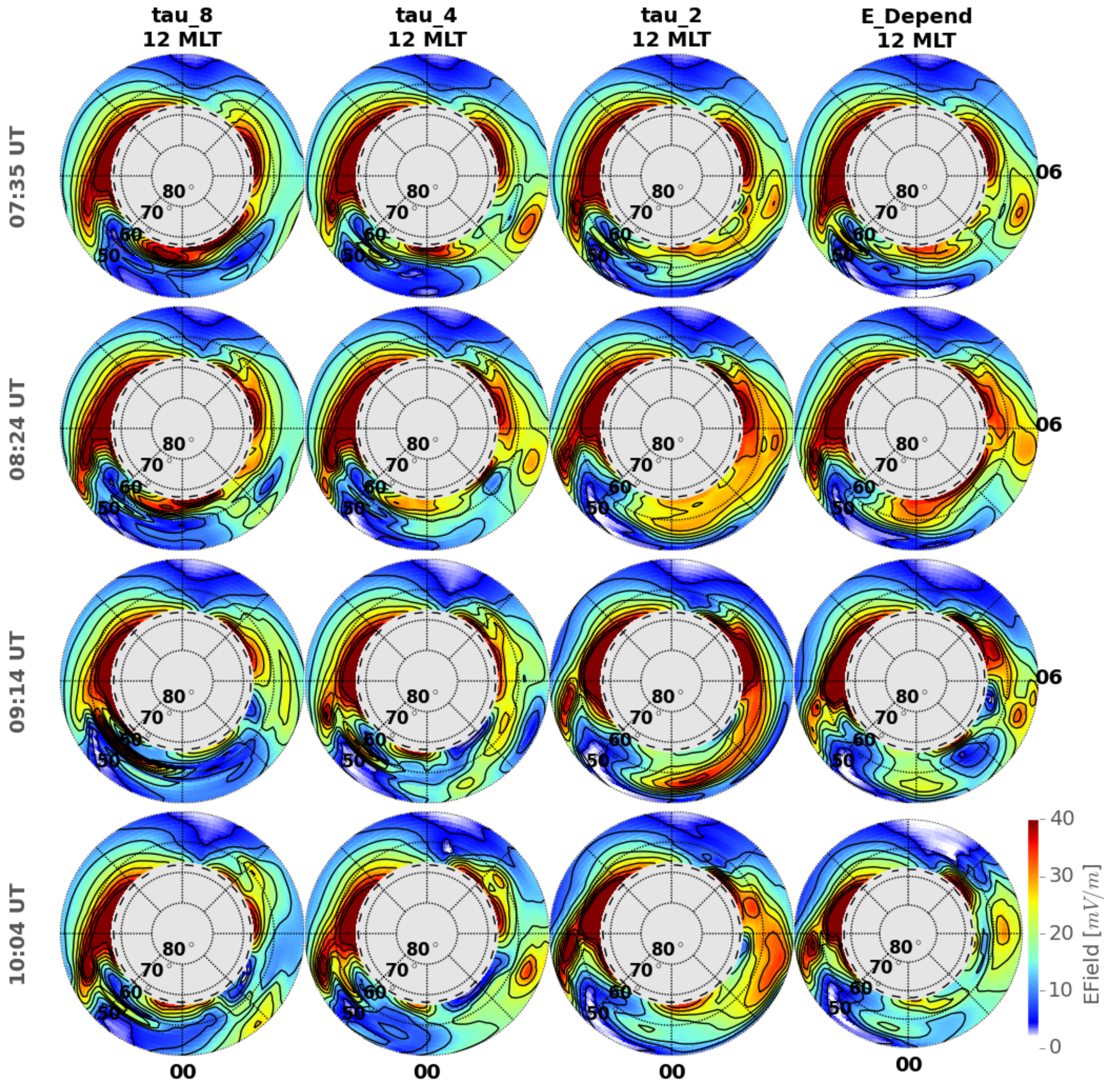

2016JA023679-f08-z-.png

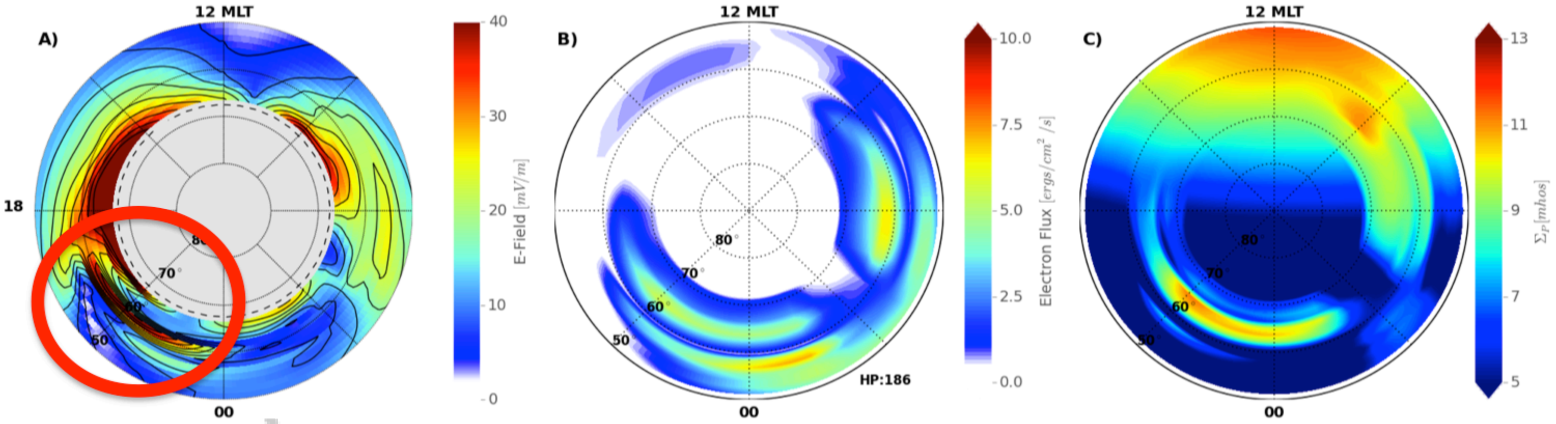

2016JA023679-f09-z-.png

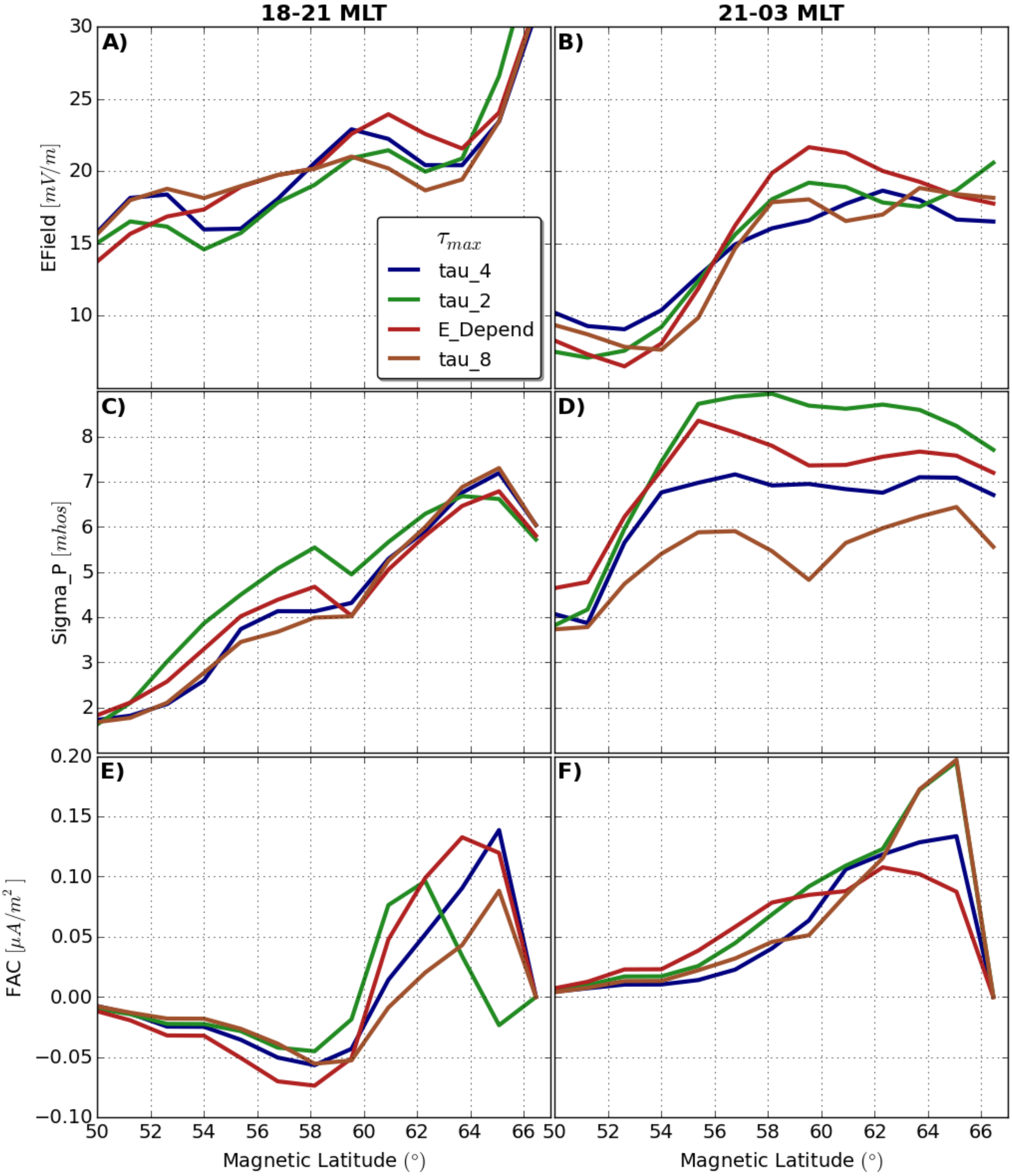

2016JA023679-f10-z-.png

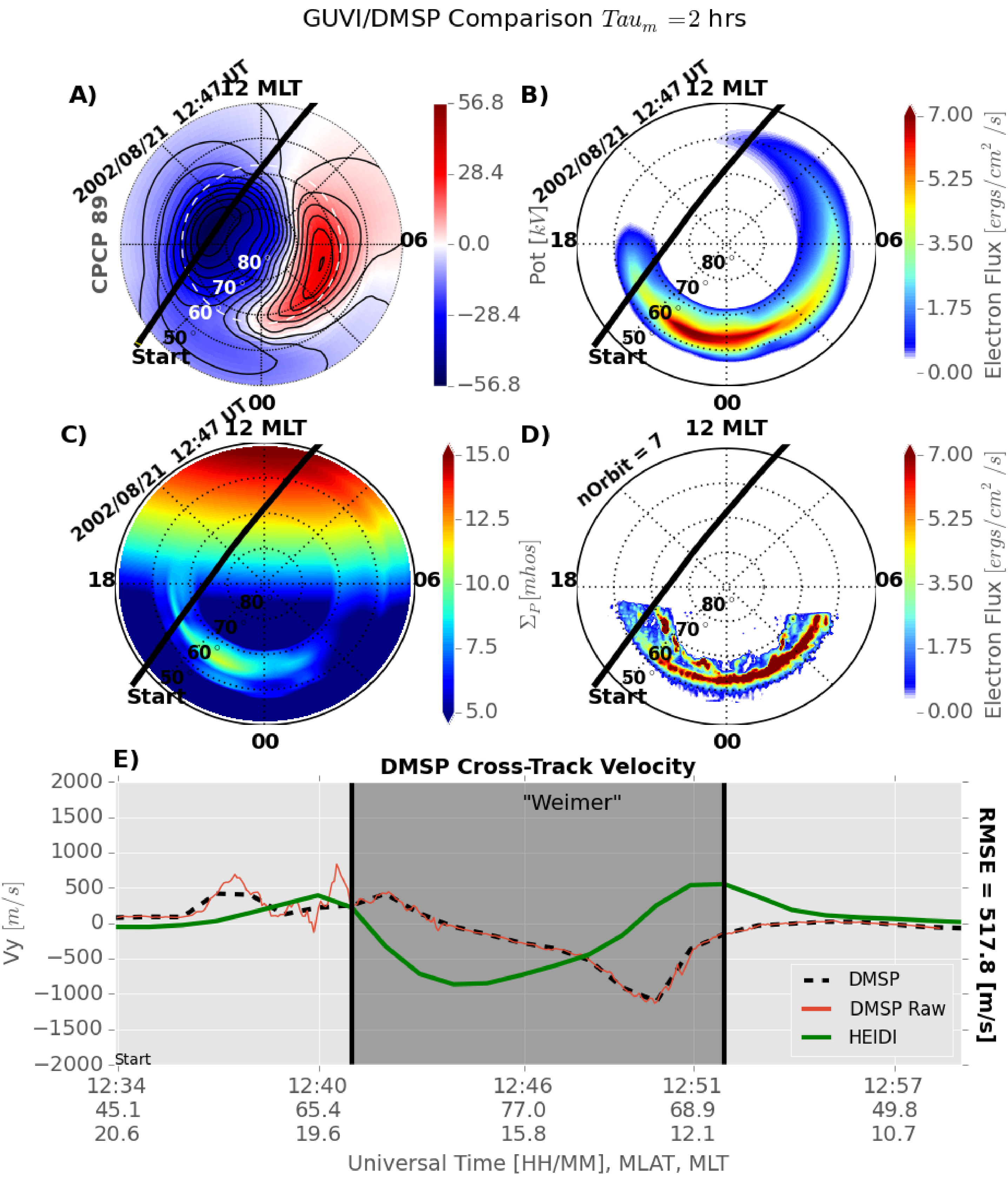

2016JA023679-f11-z-.png

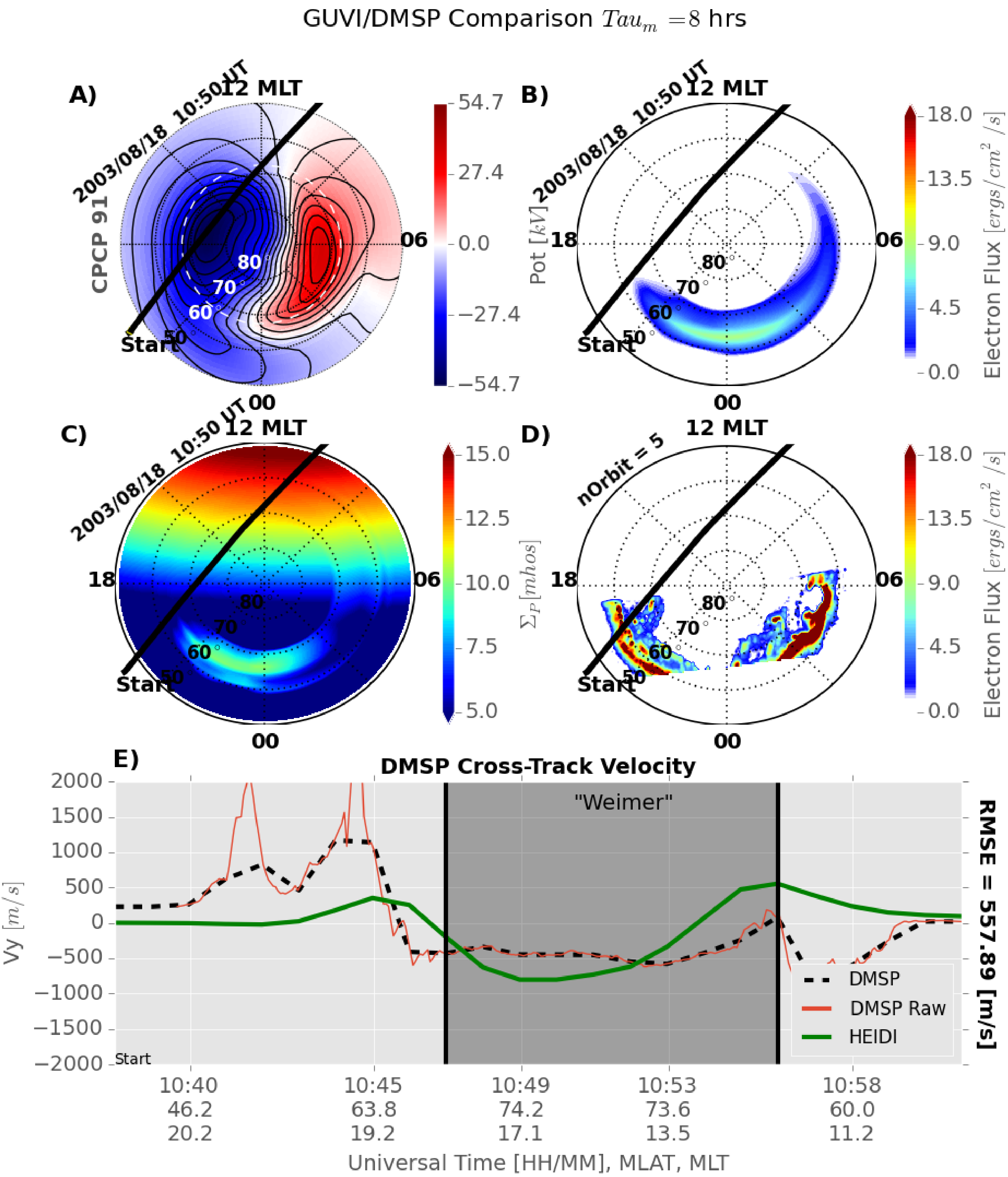

2016JA023679-f12-z-.png